Mechanical Characterization of Carbon Nanotube based Neural Probes

Spencer Roberts

A capstone report submitted to the faculty of

Brigham Young University

In partial fulfillment of the requirements for the degree of

Bachelor of Science

Robert Davis, Advisor

Department of Physics and Astronomy

Brigham Young University

August, 2020

ABSTRACT

Mechanical Characterization of Carbon Nanotube based Neural Probes

Spencer Roberts

Department of Physics and Astronomy

Bachelor of Science

Neural probes allow researchers and medical professionals to read neural activity and send signals directly to the brain. However, mechanical stiffness mismatch between neural probes and brain tissue leads to chronic irritation and trauma, which eventually causes loss of signal. Viable long-term commercial implants will require flexible probes that match the brain's stiffness. We have designed a carbon nanotube (CNT) based neural probe array that has high spatial resolution and high-aspect ratio flexible probes that have tunable stiffness via carbon infiltration. In this work, we characterize the Young's modulus of our CNT probes at various infiltration levels using a dual deflection wire test. Results indicate that the minimum modulus of the probes is about 678 MPa, which is comparable to contemporary flexible polymer probes, indicating probable long-term biocompatibility without sacrificing spatial resolution or aspect ratio.

Keywords: CNT, neural probe, biocompatibility, MEMS, elastic modulus

Acknowledgments

I would like to acknowledge the many people that helped me through this work. My wife for pulling more than her fair share during long hours of writing. Paul Minson and the BYU Microscopy department for assisting me on the SEM, Traci Neilsen for the extensive edits and writing advise. My advisors, Robert Davis and Richard Vanfleet, were instrumental in this work and would not have been possible without them. I would like to thank Dickson Bronson for assisting me in processing all this data. Finally I would like to thank the College of Physical and Mathematical Sciences for funding this project.

Contents

Table of Figures

Chapter 1: Introduction

1.1 Motivation: neural probes

The human nervous system is an amazing machine. Billions of neurons communicate through cascades of potassium, calcium, and sodium ions that generate 80 mV electrical signals called action potentials.[1] These trillions of interactions coalesce into sensory information, thoughts, and actions. The nervous system is surprisingly robust as well, capable of rerouting neural pathways to accommodate for damaged tissue or even healing the damaged neurons. However, some damage is irreparable and results in permanent handicaps. Often only the transmitting neurons are damaged while the computational power of the brain remains intact—the neurological equivalent up severing a wire to a central processing unit. Consider a blind person whose retinas or optic nerves are damaged, but their primary visual cortex is intact. If it were possible to transmit information directly to the visual cortex via a neural probe, sight could be restored.

A neural probe is any device that can communicate back and forth with the brain. The impact neural probe technology goes well beyond restoring sight. A long-term neural probe would be extremely beneficial to the medical and neuroscience community, enabling unprecedented study of neuro pathways. A fully realized neural probe would provide massive way of life improvements to the handicap community; such enabling quadriplegics to control robotic assistants organically via thought. Looking further into the future, neural probes may allow new advanced forms of entertainment, human-computer interaction, and even brain-to-brain communication. Elon Musk, founder of Neuralink, a company that is designing next

generation neural probes, said that human-machine interaction bandwidth is limited to our hands and voice, but neural probes opens up communication between man and machine to higher bandwidths[2].

Neural probes promise a great deal, but the path to implementation is complicated and difficult. The federal government has shown support for noninvasive neural interfacing[3] such as electroencephalography (EEG) , but noninvasive and minimally invasive cannot compete with the spatial and temporal resolutions possible with invasive implants. These invasive probes must be inserted during open brain surgeries that can lead to medical complications such as infection and should be kept to an absolute minimum. Therefore, once probes are inserted into the brain, they need to be stable and reliable for decades. However, current probes lack the biocompatibility and longevity to become viable chronic implants. Overcoming the challenges in spatial resolution, biocompatibility, ease of insertion, and probe longevity is the key to unlocking the vast potential of intercortical neural probes.

1.2 Literature background

Most current research uses the “Utah electrode array” (UEA) as the golden standard for invasive neural probes.[4] Developed by a group headed Richard Normann of the University of Utah, the UEA became the first FDA approved probe for human trials[5]. Using this electrode array Normann *et al.*[6] was able to measure individual neuron responses to stimuli and use this data to track eye movement in animals, an impressive achievement. Other researchers have used the UEA to implement mental control of a robotic arm.[7]

However, despite its stellar performance, the UEA still lacks the fine spatial resolution to consistently measure one neuron per electrode.[8] The spacing between the center of each probe—called the pitch—is 400 μm while the neuron pitch in the brain is about 25 μm, thereby limiting the ability to record single neuron spikes [8]. The is manufactured by dicing a silicon wafer followed by a wet etch to achieve needle-like silicon columns or probes[8]. This process produces 128 active channels per array[9] with an aspect ratio of 15:1 per individual probe.[10] However, the UEA cannot be scaled down anymore with this approach; therefore, its spatial resolution is capped.

Additionally, the individual UEA probes are very stiff and agitate the brain tissue. Chronic trauma and foreign body response have been principle hurdles to maintaining a consistent signal over long periods of time. The record for recording in vivo signals from a Utah array is nine years[5], which is an impressive record, but insufficient for commercial purposes. The chronic trauma develops as the brain moves in the skull and is irritated by the stiff probes, triggering a foreign body response. Microglial cells attack the probe site and a protein sheath develops around the probe, pushing active neurons away, increasing electrical impedance and leading to eventual loss of signal. Polymers have been proposed as a flexible probe material to address gial-scaring[11–14], but chronic longevity of polymers have not been thoroughly tested and as of 2016, the longest chronic neural recording was achieved by a silicon probe, not a polymer one.[15] Massive effort is being dedicated to develop dense arrays that satisfy the spatial requirements for single neuron recording, while keeping both acute and chronic brain inflammation and trauma to a minimum.[11]

1.3 Previous work at BYU road map

With the goal of increasing spatial resolution and decreasing inflammation, Chen *et al.*[8] from BYU used carbon nanotubes (CNT) as a novel material approach to address these issues. The BYU array developed by Chen *et al.* has a probe center-to-center pitch of 100 μm and an aspect ratio of ~60:1.[8] Physically, the UEA has 625 probes per cubic centimeter, while the BYU array can have up to 10,000 probes per cubic centimeter. The probes themselves can be up to one millimeter tall with a diameter of 40 μm, which—because of its small size—is less likely to cause inflammation.

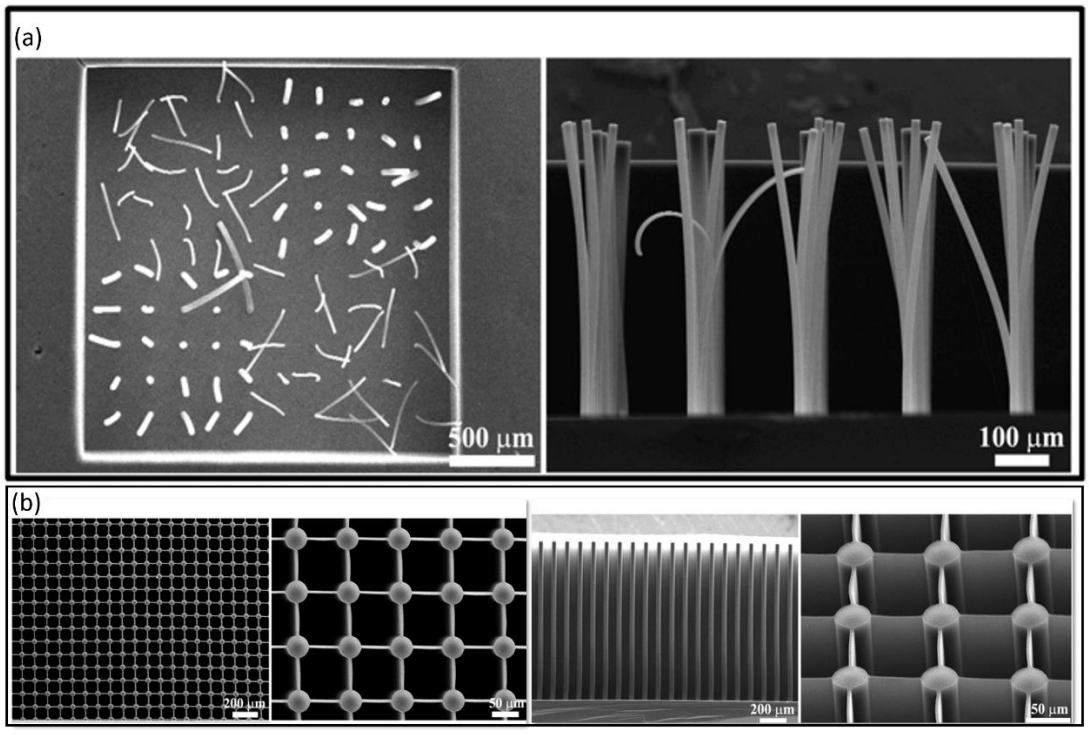

Figure 1: (a) The BYU array is unable to grow straight without supporting hedges. (b) The BYU grown tall and straight with supporting hedges.[8]

The BYU array made entirely out of millions of CNTs locked together in what is called a forest. As a whole, these forests grow together, but due to the different growth rates of individual

nanotubes in a forest, high aspect structures can begin to grow lopsided, wavy, or crooked as shown in Figure 1 part (a), unless they are self-supporting. To achieve such large probe aspect ratios, the probes must be locked into a self-supporting grid of "sacrificial hedges", as seen in Figure 1 part (b), that ensures straightness. These sacrificial hedges must be removed after growth using a multistep plasma etching process that frees the probes and narrows them to the free-standing structure in Figure 2 part (b). However, this etching process is expensive and requires a tight 100 µm spacing between probes, which is not enough room to do mechanical testing. Therefore, to do the mechanical testing detailed in this work, we opted to use shorter, unsupported probes that do not require probe-growth plasma etching and have wider 400 µm spacings.

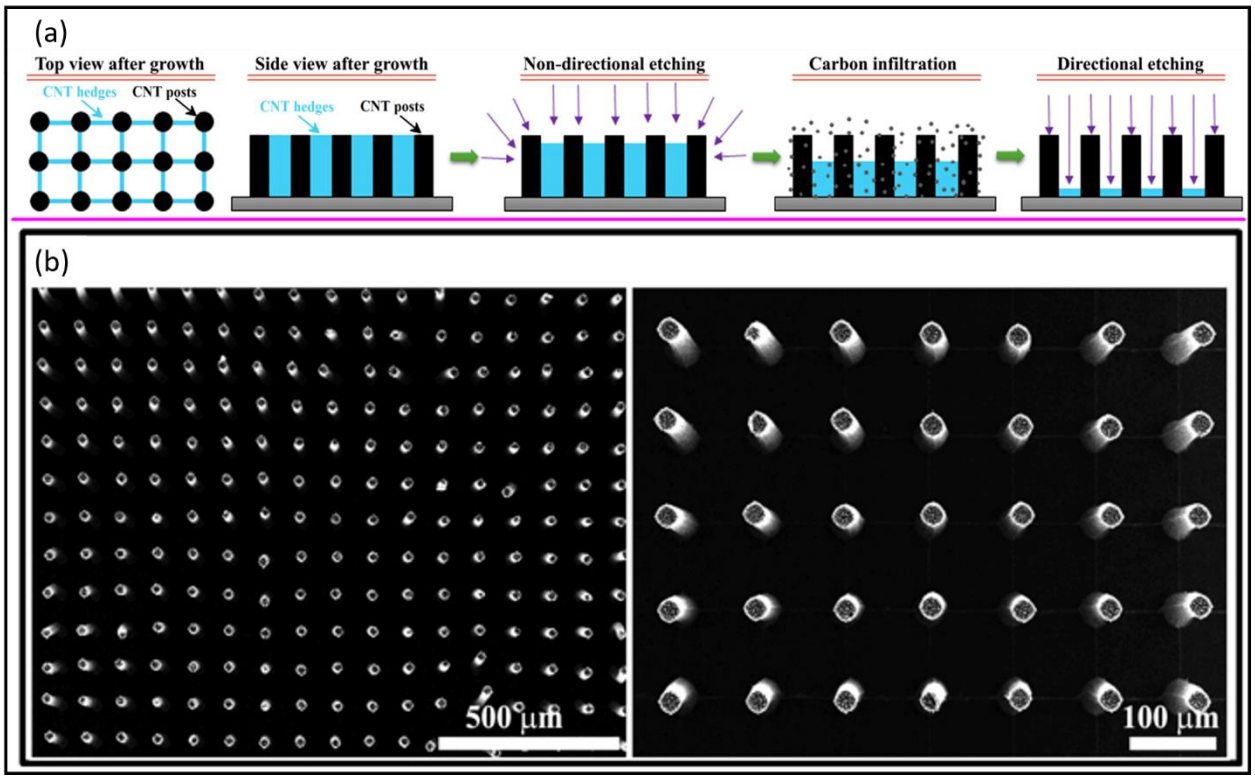

Figure 2: (a) The plasma etching process to remove the support hedges. (b) The BYU array after plasma etching away the support hedges.[8]

1.4 Overview

In this work, we test the mechanical compliance of the carbon nanotube probes by dual deflection using a thin wire. The wire pushes on the CNT probe and the deflection of both the wire and the probe are measured simultaneously (see **Error! Reference source not found.**). Then both deflections are analyzed with the Euler beam theory to convert the probe deflection to elastic—or Young's—modulus. Euler beam theory and the dual deflection test are examined in detail in sections 2.4 and 2.5, respectively.

The mechanical testing depends heavily on the geometries and materials involved; therefore, sections 2.1-2.3 examine the BYU array's unique fabrication and geometry and section 2.6 will examine how the error in the dimensional measurements propagates to the modulus calculation. First, section 2.1 will survey the general method of manufacturing CNT microstructures and section 2.2 will examine specific optimizations to our CNT growth system. Next, section 2.3 will cover the exact array growth conditions and probe geometries used in this study and compare them to the BYU array growth conditions and geometries as reported by Chen *et al.*[8] Then, section 2.6 shows how the error is calculated and shows which properties are the most dominant. Section 2.7 details how we tested the dual deflection method to ensure that its results were accurate, while section 2.8 how we attempted to independently verify the wire stiffness using 3-point bending tests on the wire. At the end of chapter 2, section 2.9 details how we processed the video footage of the test to determine the probe elastic modulus.

Chapters 3 and 4 examine the results and implications of our experiments. Section 3.1 shows the results from our growth optimization experiment and why the growth parameters in section 2.2 were used for neural probe array formation. Next, section 3.2 examines the 3-point

bending results while section 3.3 shows the method verification results and the ultimate accuracy of the dual deflection method. Then, section 3.4 reports the elastic modulus of the probes as determined by the mechanical testing detailed in section 2.5. The final section of chapter 3 examines the failure mechanisms of the CNT probes and shows several SEM images of failed probes. Then, chapter 4 discusses the how the uncertainty sensitivity affects the results of section 3.3 and evaluates whether the CNT probes can function as a more biocompatible neural probe material and any additional challenges that might prevent commercialization. Finally, this work concludes with additional work that needs to be done with the BYU array to bring it closer to clinical use.

Chapter 2: Methods

2.1 Carbon nanotube Micro-Electro-Mechanical Systems

The CNT manufacturing process can produce extremely fine, sharp structures that can function as micro-electro-mechanical systems (MEMS). This manufacturing process was developed at BYU by Hutchinson *et al.*[16], using well known CNT MEMS manufacturing techniques, including thin film evaporation, cleanroom photolithography, and catalytic chemical vapor deposition (CVD). This section will review the nature of CNTs, the general process of CNT growth, and the specific parameters used to produce CNT MEMS in our experiment.

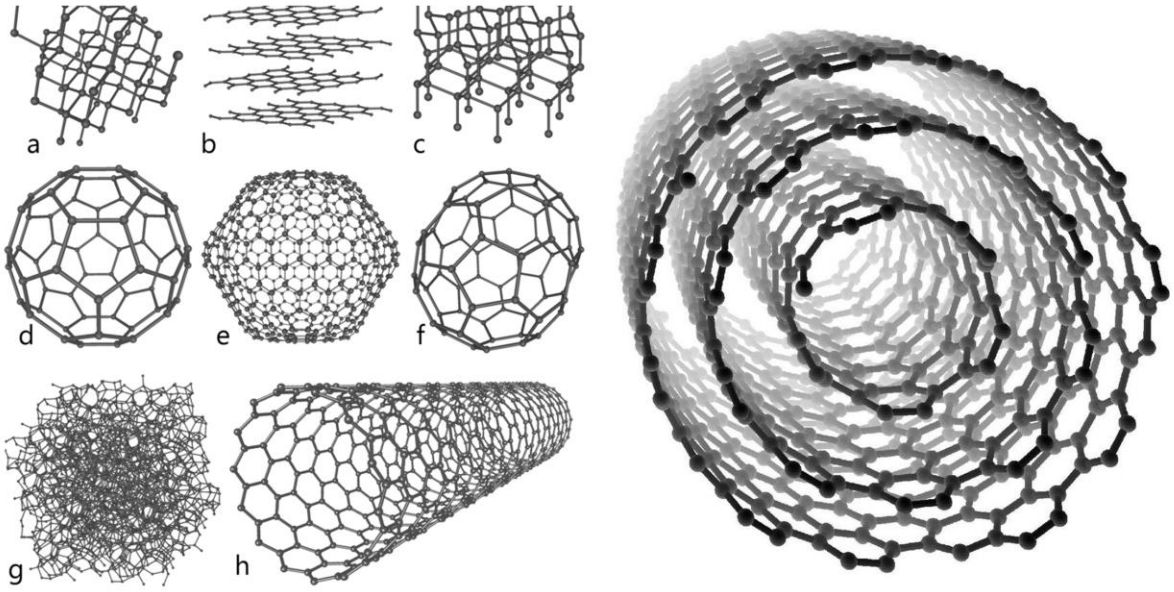

Figure 3: Left: Eight of the allotropes (different molecular configurations) that pure carbon can take: a) Diamond b) Graphite c) Lonsdaleite d) C60 (Buckminsterfullerene) e) C540 f) C70 g) Amorphous carbon h) single-walled carbon nanotube. Credit Michael Ströck.[17] Right: A multi-walled carbon nanotube.[18]

A CNT is a unique allotrope, or chemical alignment, of pure carbon atoms. It is composed of repeating hexagonal units and resembles a graphene sheet—shown in Figure 3.b—that has been rolled into a tube. There are two types of CNTs: single-walled carbon nanotubes (SWCNT) and multi-walled carbon nanotubes (MWCNT). A SWCNT is depicted in Figure 3.h and a MWCNT is depicted on the right in Figure 3. These two classes of CNTs have different attributes and grow under different conditions, but all CNTs possess many unique and desirable qualities, such as: electrical conductivity, extreme strength-to-weight ratios over 100 times greater than high-carbon steel, high optical absorption, and good thermal conductivity[19]. Growth conditions can be tuned to control these properties by altering how many walls the tube has and its chirality, *i.e.*, the angle of the graphene wall of the CNT. While individual nanotubes are fascinating materials, this work utilizes CNTs grown as a tight knit "forest", which can be

patterned after any two-dimensional pattern with techniques detailed later in this section. These forests allow for the manufacturing of tight dimensions necessary for MEMS and take advantage of CNT electrical conductivity on a microscale. Figure 4, a CNT forest in the shape of the BYU logo, shows the complex patterning capability of CNT MEMS as well tight dimensional control and fine features.

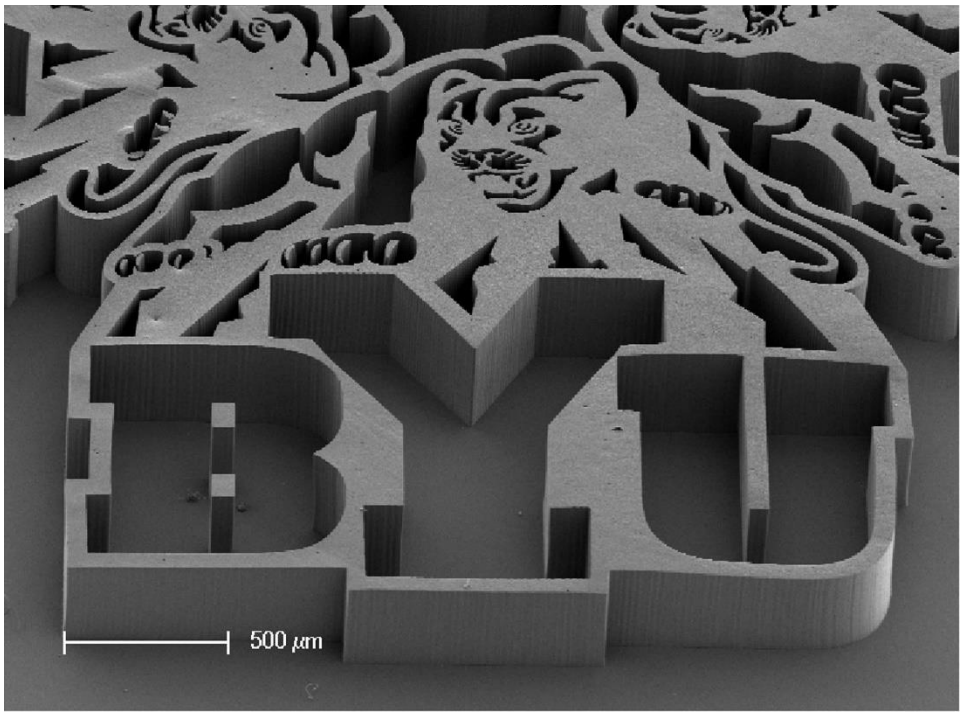

Figure 4: A carbon nanotube forest patterned in the shape of the BYU logo. Picture taken by Taylor Wood.[20]

Carbon nanotube growth is very sensitive to many parameters, especially the nature of the thin film stacks on the growth substrate. CNT-M (carbon nanotube templated microfabrication) relies on specific thin film catalyst stacks for patterned CNT growth, which are shown in Figure 5. The orange film shown in Figure 5 is the catalytic metal on the surface of the stack upon which CNTs grow. The catalyst must be thin for CNT growth to occur: between 2 and 10 nm. In our method, we used 2 nm of iron—the most common CNT catalyst—for CNT growth. Evidence has shown that there when the iron layer is thinner, the CNTs grow fast and

die young and that relationship inverts as the iron gets thicker.[21] The growth process occurs at 750˚C and at that temperature, the iron begins to form small droplets on the surface. Similar to soap bubbles on the surface of water, the larger iron droplets begin to grow at the expense of the smaller ones, consolidating the iron into large droplets; this process is called Ostwald Ripening[22]. As the droplets get bigger, the CNT's diameter grows bigger and the tubes grow much slower. However, if the iron layer is placed on top of an alumina layer, the lateral diffusion of the iron is limited, keeping the droplets and the CNT diameters small.

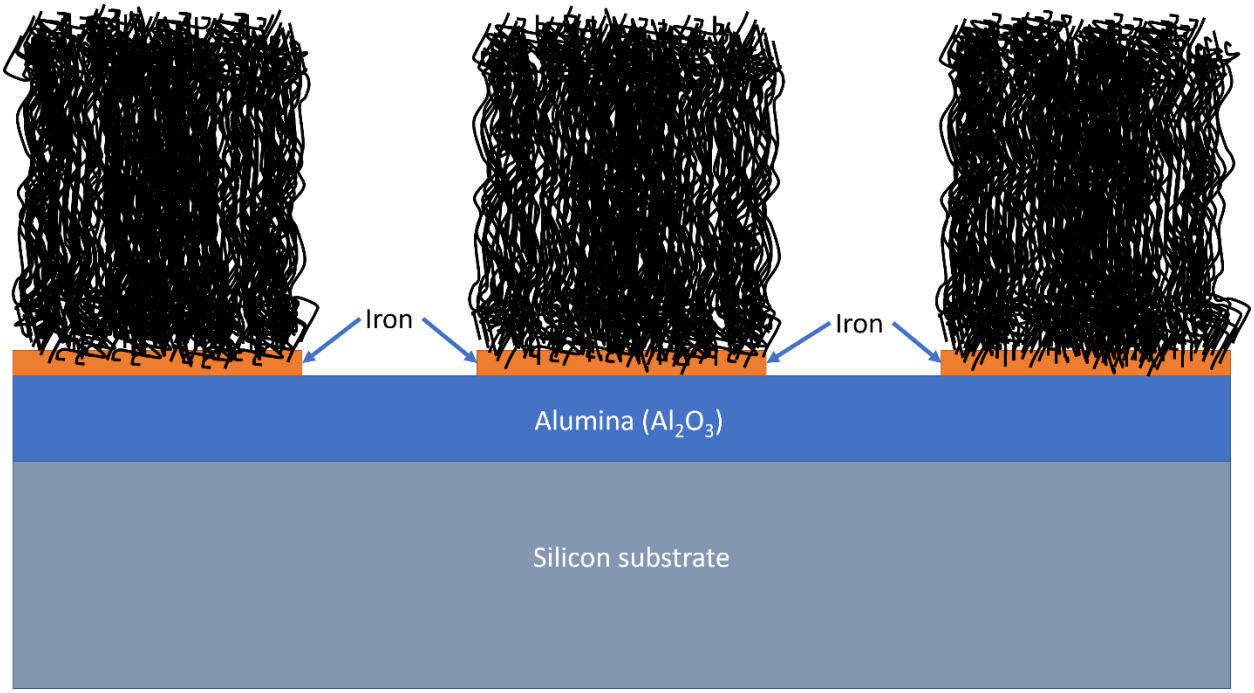

Figure 5: A depiction of the thin film stack required for CNT MEMS growth. The CNTs grow directly out of the iron.

The alumina layer also helps prevent the diffusion of the iron droplets into the layers below them, a growth termination mechanism that decreases the amount of available catalyst.. CNT forests are usually grown on a standard commercial grade silicon wafer of any size. A thin film of alumina (*see Figure* 5) approximately 40 nm thick is deposited on the silicon surface in a cleanroom setting via electron beam (e-beam) evaporation or sputtering. E-beam evaporation

uses a strong electron beam to melt and evaporate material onto any target surface above the melted source, while sputtering uses accelerated ions to blast matter off a target source and deposit it on a substrate. Even though each method produces different thin film morphologies, both produce alumina layers suitable for carbon nanotube growth. The alumina layer is an important insulating layer between the silicon wafer and the iron film on which the CNTs grow. Without the alumina barrier, the iron would quickly diffuse into the silicon when exposed to heat. The alumina slows this diffusion process, keeping the iron on the surface long enough for carbon nanotubes to form.

Once the alumina layer is deposited, the catalytic iron layer can be deposited. If iron is deposited over the entire surface of the alumina, then CNTs will grow over the entire surface, making a "blanket" forest without any patterns or features. This blanket growth is used for the experiment detailed in section 2.2. If a patterned forest is desired, like Figure 1 and Figure 4, then the silicon/alumina stack is coated in AZ3030, a positive photoresist, then exposed to UV light through a patterned mask that casts a shadow in the shape of the desired 2D growth pattern. The wafer is immersed in developer which removes the unexposed photoresist, leaving behind holes in the pattern we want. Iron is then deposited on the wafer and the remaining photoresist is removed with an organic solvent (NMP). The result is a silicon/alumina/iron stack where the iron is patterned in a top down view of our desired 3D structure. The CNTs will grow directly on top of the patterned iron.

This stack is then placed in a CVD furnace and heated to 760 C˚ while hydrogen continually flows over the sample, reducing the iron on the surface, to prep for CNT growth. Once the target temp of 760 C is met, ethylene flows as a carbon feed stock gas, which breaks down under the heat and deposits on iron in catalytic fashion. The iron promotes rapid CNT

growth, producing up to one mm in 15 minutes in our system. Once the target time is met, the system is cooled under argon flow and the sample is removed. The resulting sample is a 3D CNT projection of the 2D photolithographic pattern, as seen in Figure 1, Figure 4 and Figure 5.

Finally, the CNT structure is strengthened with carbon infiltration. As grown, the CNT forest is mostly void, which can make it very fragile to the touch. Filling the voids to some degree with amorphous carbon greatly strengthens the structure so that it can survive mechanical testing. Infiltration is done with the same growth conditions but at higher temperatures between 800˚C and 900˚C. The exact conditions of the infiltration used for this work are detailed in section 2.3.

2.2 CNT growth optimization

Despite years of research, carbon nanotubes are still difficult to grow with consistent quality. CNT forests have a tight window for optimal growth and are very sensitive to slight changes in conditions such as water content in growth chamber, gas flow rate, gas ratio, temperature, iron thickness, thin films stacking order, substrate material, alumina morphology, annealing time, temperature ramp rate, growth temperature, etc. As such, each individual system needs to be optimized to achieve tall growths. Tall CNTs are necessary for neural probes to penetrate the cortex deeply enough to get good signal and access neurons deeper in the brain.

However, since CNT growth is so complex, testing all the possible variables is not possible. Therefore, in optimizing our system, my colleagues and I limited the variables tested to four, which—considering the extensive list above—was no easy feat. First, we limited our search to parameters that experienced frequent fluctuation and, thus, significantly narrowed the possible optimization parameters. Next, we looked at what we could easily control with some accuracy.

This eliminated variables like water content, which we know has a large impact on growth[23], but would require extensive modifications to our growth system to properly control. After these eliminating steps, we settled upon four variables that fit the following criteria: they were easily controllable, had a well-tested starting value, and were indicated by literature to have a large impact on CNT growth.

After choosing our four parameters—gas flow rate, hydrogen to ethylene ratio, growth temperature, and iron film thickness—we needed to decide how to execute our experiment. First, we picked which values of each parameters to test. If we used wide range of values for each parameter, we could get a very complete picture of the impact each parameter has on growth height, but depending on how we designed the experiment, each value, or state, that we add to the parameters can dramatically increase cost. Consequently, the careful design of experiment is supremely important.

Design of experiment (DOE) is branch of applied statistics that applies statistical methods to the planning, execution, and analysis of tests, "designed to model and explore the relationship between factors and one or more responses."[24] There are a wide variety of experimental designs that screen for different relationships between factors and responses. Some DOEs are better for signal-to-noise analysis while others focus on second order factor interactions. We decided to use what is called a factorial design, *i.e.*, a screening method that looks at the first and higher order interactions of factors on a response. Factorial designs are designed to be orthogonal, meaning that the estimate of each effect is independent of the other estimates. Factorial designs that are orthogonal for all effects are called full factorial designs. A full factorial design has as many runs, or sample size, as the product of the values, or levels, of the factors, as shown in equation 2.2.1, where S is sample size, L is the number of levels per factor, and k is the number of factors.

$$S = L^k \tag{2.2.1}$$

With a full factorial design, as factors and levels are added, the sample size increases quickly, quickly reaching beyond a reasonable sample size. For example, if four factors with two levels each were to be studied—a reasonable study—then the sample size would be:

$$S = 2^4 = 16 \tag{2.2.2}$$

However, if just one level is added to each factor, the sample size jumps to 81. Note that this number does not include any repeat studies, which important to show repeatability. A good rule of thumb is to repeat an experiment three times to determine repeatability. With three repeat experiments, the total number of runs necessary is 48 for the two-level and 243 for the three-level. Obviously, this can get out of hand quickly, so limiting the levels to two-level is vital.

We can also limit the sample size by using what is called a fractional factorial design, instead of a full factorial design. A full factorial design will detail a full resolution of all the interactions up to the order of the number of factors. But it is rare that third order and higher interactions are of interest since most of the response will be dominated by main factors and second order interactions. This makes full factorial designs an inefficient use of resources. A fractional factorial design is defined by equation 2.2.3.

$$S = L^{k-p} \; where \; p < k \tag{2.2.3}$$

When using a two-level fractional factorial design, each increase in *p* halves the sample size. This downsizing causes the higher order effects to be *confounded* with other effect, making them indistinguishable. But since higher order interactions effects are most often negligible, the tradeoff is desirable. Therefore, we decide to use a fraction factorial design with $p = 1$ such that

our sample size was reduced from 16 to 8, with three repeats, for a final total of 24 runs. For more information on Design of Experiments and factorial design, see the SAS Institute's "Design of Experiments Guide". [24]

After choosing a two-level fraction factorial design, we had to identify the two levels of each factor to test. Since we only selected factors that had a well-defined value that was currently used in our growth recipe, we could use that value as a starting point for selecting reasonable high and low levels that would likely promote strong CNT growth. Table 1 contains the starting values of each factor as well as the selected levels.

	Growth Temperature (˚C)	*Gas flow rate (sccm)*	*Gas ratio (H_2:C_2H_4)*	*Iron thickness (nm)*
Original value	750	~650	1	4
Low level	740	500	0.9	2
High level	760	800	1.1	4

Table 1: The factors and levels of the factional factorial growth experiment detailed in section 2.2

Once we had our high and low levels, I designed a fractional factorial experiment in SAS JMP statistical analysis software that would analyze the first order and second order effects of temperature, gas flow rate, gas ratio, and iron thickness on CNT forest height. JMP then produced an eight-run permutation of the levels which we ran three times with square blanket growth samples.

After each run, the sample's forest height was measured optically and in the Scanning Electron Microscope (SEM). To measure them optically, we used an Olympus optical microscope and measured the height at each corner and in the center of the forest relative to the substrate surface. To measure them in the SEM, we would cleave the sample in half and view at a 90˚ angle and take a line measurement as shown in Figure 6. All measurements on a sample were averaged and the average was inputted into JMP, which plotted the log worth—the negative log of the p value—of each main effect and the three most impactful second order interaction effects. The measured heights and JMP's statistical analysis are detailed in section 3.1, as well as the specific growth recipe determined by the study to produce tall growths suitable for neural probes.

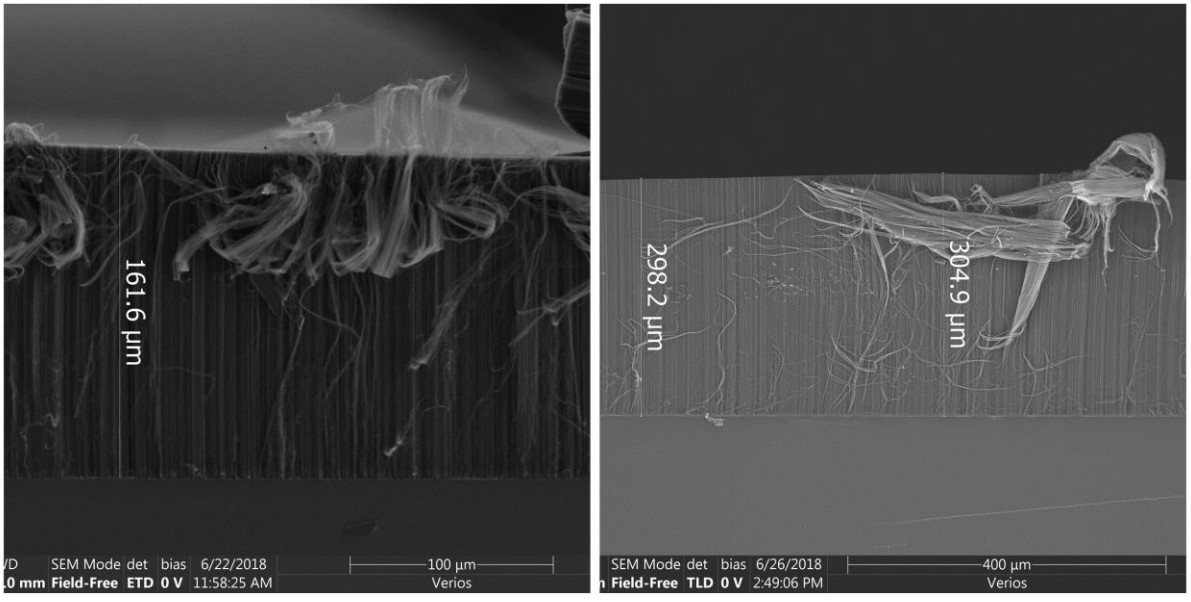

Figure 6: Cleaved CNT forests measured at 90˚ in a SEM.

2.3 Probe geometry and fabrication

Much of our neural probe fabrication process and geometry has already been explained in sections 2.1 and 1.3 respectively, so this section will emphasize the exact characteristics of the samples used for mechanical testing. Since the plasma etching process used by Chen *et al.*[8] is expensive and requires 100 μm pitch between probes, we opted to use shorter probes with a pitch of 400 μm that could be grown straight without sacrificial hedges as seen in Figure 2. Despite growing shorter probes, we opted to use the optimized growth formula determined by the study detailed in section 2.2. A complete comparison between the specifications and growth formula of the Chen *et al.*[8] neural array and the array I used for mechanical testing are detailed in Table 2.

		Chen et al. *array*	*Array used for this thesis*
Growth	Growth temperature (˚C)	750	760
	Gas flow rate (sccm)	~480	~500
	Gas ratio (H_2:C_2H_4)	1	1.1
	Iron thickness (nm)	4	2
	Infiltration (˚C and minutes)	900, 1.5	900, 0.5
Geometry	Height (μm)	~1300	600 - 500
	Probe diameter (μm)	40	40
	Center-to-center Pitch (μm)	100	400
	Support hedges	Yes	No
	Plasma etch	Yes	No

Table 2: A comparison of growth conditions and geometry of the Chen *et al.* array and the array used in this work

2.4 Euler beam theory

The theoretical basis for measuring beam stiffness using deflection under force is the Euler beam theory. This beam theory applies only to small beam deflections under lateral loads, which are the conditions used to test the probes as detailed in section 2.5. The theory starts by

relating the bending moment to the curvature or deflection of the beam. The bending moment equation is a well-known and important engineering equation and for those interested, there is full derivation on Wikipedia.[25] The bending equation is shown in equation 2.4.1, where M is the bending moment, E is the elastic modulus of the beam, I is the second moment area of the beam's cross-section, and $\frac{\partial^2 y}{\partial x^2}$ is the second derivative of the beam deflection with respect to some position x.

$$M = -EI\frac{\partial^2 y}{\partial x^2} \tag{2.4.1}$$

For cantilevered beam—a beam that is clamped at one end—the bending moment is also equal to equation 2.4.2, where F is the lateral force on the end of the beam, L is the length of the beam and x the distance from the clamp to the end of the beam. From 2.4.2, we see that the bending moment is maximum at the base of the beam and zero at the end of the beam.

$$M = -F(L - x) \tag{2.4.2}$$

By setting equations 2.4.1 and 2.4.2 equal to each other, integrating, and evaluating at $x = L$, the free end deflection is obtained in equation 2.4.6.

$$\frac{\partial^2 y}{\partial y^2} = \frac{F}{EI}(L - x) \tag{2.4.3}$$

$$\iint \frac{\partial^2 y}{\partial x^2} = \iint \frac{F}{EI}(L - x)\, dx^2 \tag{2.4.4}$$

$$y = \frac{F}{6EI}(3Lx^2 - x^3) \tag{2.4.5}$$

$$y = \frac{FL^3}{3EI} \tag{2.4.6}$$

Now by Hooke's law, the stiffness of a spring is the force applied to it divided by the distance that it the spring deflects. Therefore, equation 2.4.6 is easily rearranged to find the elastic modulus with respect to the beam's stiffness, k.

$$E = k\frac{L^3}{3I} \tag{2.4.7}$$

Finally, the second area moment, I, for a beam with a circular cross-section, is equal to $\frac{\pi d^4}{64}$, where d is the diameter of the beam. This substitution yields equation 2.4.8, the final description of the beam's elastic modulus with respect to stiffness. However, for our experiment, the only experimentally measured values are deflections. Therefore, we will include force and deflection in our final result, as shown in equation 2.4.8.

$$E = \left(\frac{F}{y}\right)\frac{64L^3}{3\pi d^4} \tag{2.4.8}$$

2.5 Dual deflection method

To measure the modulus of a probe using the Euler beam theory, we designed an experimental set up where we can apply a lateral force to the probes via a small wire and record the deflection of both the wire and probe under a microscope. Figure 8B shows a 3D schematic of this interaction. Both the wire and the post will obey equation 2.4.8 and since they both deflect in the same interaction, we can equate their forces as show in equation 2.5.1. We can linearize this equation as shown in equation 2.5.2 which equates the deflection of the post, y_p, to the deflection of the wire, y_w, by a constant. The constant is show in equation 2.5.3 to be A/R,

where A is determined by the length and diameter of the post and wire, while R is the ratio of their respective moduli. Upon graphing $y_p\ vs.\ y_w$ (equation 2.5.2), we can fit the data to a linear regression and set the obtained slope equal to A/R, as shown in equation 2.5.4. Since A is a known constant, we can solve for R using the slope and then use R to calculate the post elastic modulus as shown in equation 2.5.5. The relative uncertainties in $m, A,$ and R and their effect on the final elastic modulus of the post are detailed in section 2.6.

$$\frac{E_w y_w 3\pi d_w^4}{64\ L_w^3} = F = \frac{E_p y_p 3\pi d_p^4}{64 L_p^3} \tag{2.5.1}$$

$$y_p = \left(\frac{E_w}{E_p}\right)\left(\frac{d_w^4 L_p^3}{d_p^4 L_w^3}\right) y_w \tag{2.5.2}$$

$$y_p = \frac{A}{R} y_w, \qquad A = \left(\frac{d_w^4 L_p^3}{d_p^4 L_w^3}\right), \qquad R = \left(\frac{E_p}{E_w}\right) \tag{2.5.3}$$

$$m = \frac{A}{R}, \qquad R = \frac{A}{m} \tag{2.5.4}$$

$$E_p = R E_w \tag{2.5.5}$$

The experimental set up to measure the deflection of the post and wire is show in **Error! Reference source not found.**Figure 7 and **Error! Reference source not found.**A. In Figure 7, the small black square under the microscope, denoted by 1), is the CNT neural probe sample. The sample is elevated from the microscope stage to accommodate the wire apparatus, which is denoted by 2). A thick wire extends from the clamp and the small Stablohm wire is glued to it using Elmer's glue. The wire is fixed in space and maintained in focus under the microscope. The wire clamp is secured to a three-axis stage that is suspended by a metal arch via magnets which rests on the tabletop with the microscope. The sample, via the microscope stage, is brought up into focus and moved to position the wire near the top of a single probe. A camera records the entire process through the microscope at 30 frames a second in HD. The arch and

camera are shown in Figure 7. The magnification of the scope is low enough so that a neighboring post can be viewed as a reference as shown in Figure 12. The reference is used to calculate the distance the post moves since it is the sum of the wire and post deflections, which is demonstrated in Figure 8B and shown in equation 2.9.1. The details of how the post deflection is calculated are explained in section 2.9

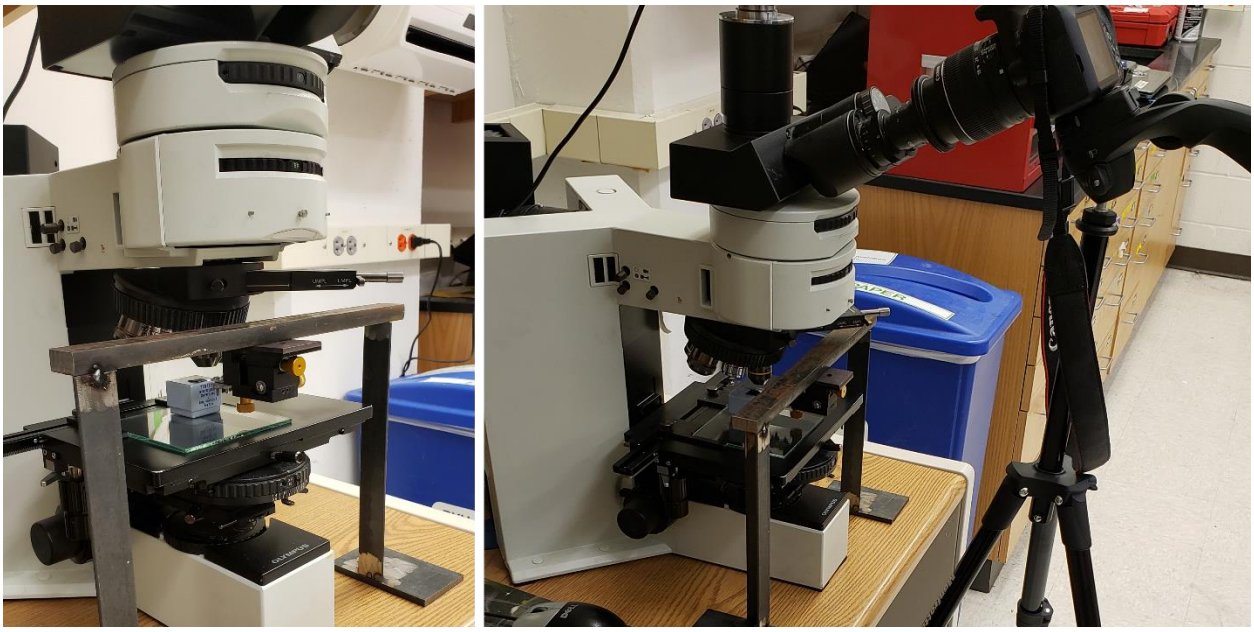

Figure 7: The dual deflection mechanical testing set up. Left: The metal arch suspends the 3-axis stage that holds the wire. Right: The camera records the wire/probe deflection directly through the microscope lens.

Once the wire and sample are in place, precise positioning of the probe relative to the wire is necessary for an accurate measurement. First, the view is focused on the substrate surface and then advanced upward until the top of the target probe is in focus, thus marking the height of the probe. A quick scan over all the target probes in that row to check if they are in focus, *i.e.*, they are the same height as the first measured probe is done to speed up testing. Since length is an important variable for the Euler beam theory, all the probes must have a precise height measurement. If any of the probes in a target row are out of focus, they must be individually measured for height. Once all the heights are recorded, the sample is positioned with the first

probe in the row right next to the wire, which should be perpendicular to the row of probes. The sample is shifted until both the top of the probe and the top of the wire are in focus. Then the probe is moved up so that the top of the wire is between 10 and 50 μm from the top of the probe (y). The distance from the substrate to the middle of the wire is calculated by adding half the diameter of the wire, $d/2$, to y and subtracting that number from height of the probe (h_p). This position is called $h_w = wire\ height$ as shown in equation 2.5.6 and is the effective height of the probe since it is where the wire applies force to the probe.

$$h_w = h_p - \left(y + \frac{d}{2}\right) \qquad 2.5.6$$

Once the probe is touching the wire at the correct height, force may be applied. The stage is slowly moved horizontally to push the probe into the wire causing deflection as show in **Error! Reference source not found.**Figure 8B. In the figure, the horizontal cylinder represents the wire—which is fixed in space—while the vertical cylinder, the probe, moves underneath it. The two cylinders begin to deflect under the force until the probe fails. The next probe is then moved into contact with the wire and since both the probe height already measured and relative height of the wire is held constant, the next test can proceed immediately. The process repeats until all the target probes are measured. After all the probes are measured, the sample is put into the scanning electron microscope (SEM), and the broken posts are imaged to examine the failure mechanisms. The SEM images are shown in section 3.5.

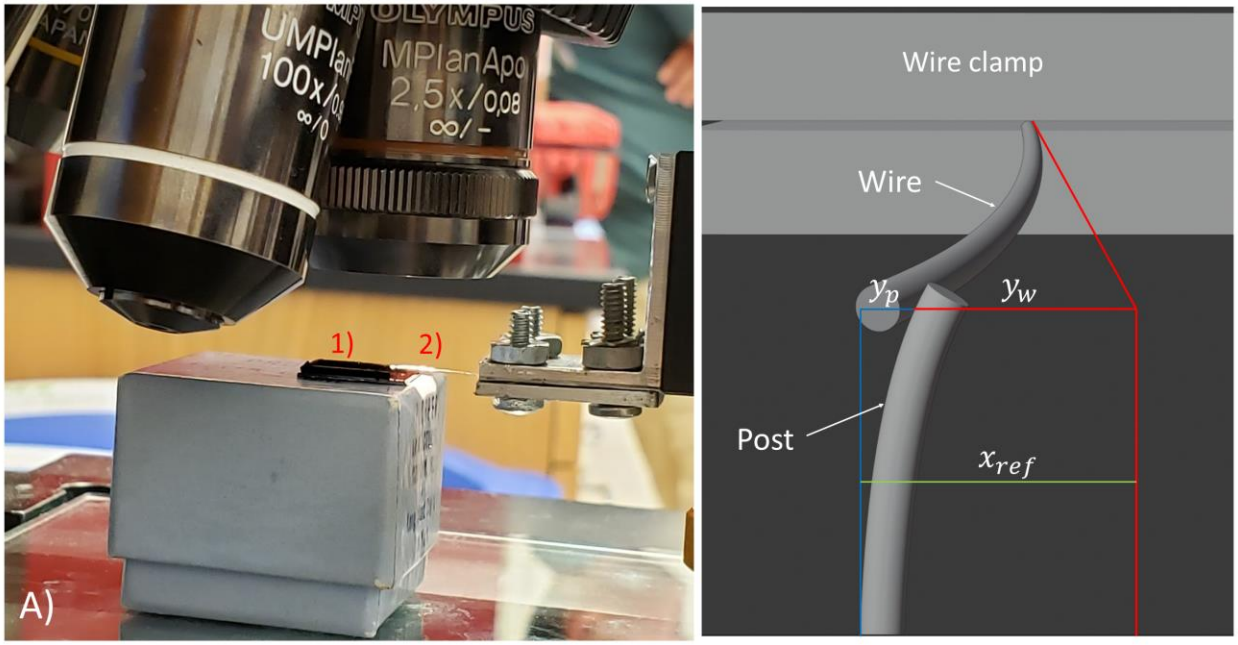

Figure 8: A) The dual deflection experimental set up. 1) neural probe CNT sample 2) Stablohm wire. B) A 3D representation of the measured deflections of the probe, y_p, and wire, y_w. The red and blue lines indicate the original positions and deflections of the wire and post respectively. The green line x_{ref} is the total distance traveled by the reference post.

2.6 Error Analysis

As with all physical experiments, the usefulness of the experimental data is contingent upon the accuracy of measured values and their error bars. Since the scale of our experiment is very small, we are limited in how accurately we can measure physical quantities. Equation 2.5.3 shows the variables needed for linearization and calculation of the post modulus; A is comprised of all the dimensional quantities of the wire and posts, R contains the wire elastic modulus, and y_w and y_p are the independent and dependent variables respectively. The quantities we measured—shown in Table 3—are as follows: reference displacement, wire deflection, wire diameter, post diameter, post full length, post length offset, wire full length and wire offset length. Remember that the post deflection is not a directly measured quantity but is difference between the reference displacement and wire deflection, as indicated in equation 2.9.1. The post

length and wire length follow similar equations in 2.6.4 and 2.6.5. The wire elastic modulus is provided by the manufacturer and is also included in Table 3. All these quantities carry an uncertainty or variation with them. These variations propagate through the math shown in equations 2.5.2 – 2.5.5 and ultimately become an uncertainty in the post modulus.

The principles of simple error propagation rely on the assumption that the errors in the measured quantities are uncorrelated or random. With this assumption, there are three error propagation formulas that relevant to our method: addition and subtraction (eq 2.6.1), multiplication and division (eq 2.6.2), and raising to a power (eq 2.6.3).

$$(a \pm \Delta a) \pm (b \pm \Delta b) = c, \qquad \Delta c = \sqrt{\Delta a^2 + \Delta b^2} \tag{2.6.1}$$

$$ab = c \; or \; \frac{a}{b} = c, \qquad \frac{\Delta c}{c} = \sqrt{\left(\frac{\Delta a}{a}\right)^2 + \left(\frac{\Delta b}{b}\right)^2} \tag{2.6.2}$$

$$a^n = c, \qquad \frac{\Delta c}{c} = n\frac{\Delta a}{a} \tag{2.6.3}$$

Using these error propagation formulas, we calculate the contributions of the variation in the base quantities on the post modulus. These error propagations are shown in equations 2.6.4 – 2.6.9. However, equation 2.6.8 shows that we need to know ΔR to find ΔE_p and to find ΔR we need to know Δm, where m is the slope of equation 2.5.3. To find m, we need to do a linear regression on equation 2.5.3. The most common and simple method of doing a linear regression is an Ordinary Least Squares (OLS) method, which assumes that there is little to no uncertainty in the independent variable, in our case, the wire deflection, y_w. But there is variation in the y_w measurements, so we cannot use an OLS method. Instead, we use a model called Deming regression, which accounts for error in both x and y. The Deming model consolidates x and y

error into a single ratio, $\lambda = \Delta x/\Delta y$, so the only the relative values of the error matter. The wire deflection uncertainty, Δy_w, is an intrinsic value, while Δy_p is calculated in equation 2.6.9. These values, along with λ, are listed in Table 3. The Deming regression model, calculated in Excel using the Real Statistics package, outputs the slope of the regression, as well as the uncertainty, Δm.[26] With these outputs, we can solve equation 2.6.7 and consequently equation 2.6.8.

$$L_w = L_{w_{full}} - L_{w_{offset}}, \qquad \Delta L_w = \sqrt{\Delta L_{w_{full}}^2 + \Delta L_{w_{offset}}^2} \tag{2.6.4}$$

$$L_p = L_{p_{full}} - L_{p_{offset}}, \qquad \Delta L_p = \sqrt{\Delta L_{p_{full}}^2 + \Delta L_{p_{offset}}^2} \tag{2.6.5}$$

$$A = \left(\frac{d_w^4 L_p^3}{d_p^4 L_w^3}\right), \qquad \frac{\Delta A}{A} = \sqrt{\left(4\frac{\Delta d_w}{d_w}\right)^2 + \left(3\frac{\Delta L_p}{L_p}\right)^2 + \left(4\frac{\Delta d_p}{d_p}\right)^2 + \left(3\frac{\Delta L_w}{L_w}\right)^2} \tag{2.6.6}$$

$$R = \frac{A}{m}, \qquad \frac{\Delta R}{R} = \sqrt{\left(\frac{\Delta A}{A}\right)^2 + \left(\frac{\Delta m}{m}\right)^2} \tag{2.6.7}$$

$$E_p = RE_w, \qquad \frac{\Delta E_p}{E_p} = \sqrt{\left(\frac{\Delta R}{R}\right)^2 + \left(\frac{\Delta E_w}{E_w}\right)^2} \tag{2.6.8}$$

$$y_p = \left|y_w - x_{ref}\right|, \qquad \Delta y_p = \sqrt{(\Delta y_w)^2 + \left(\Delta x_{ref}\right)^2} \tag{2.7.9}$$

2.7 Dual deflection method verification

In order to have confidence in the data produced by the dual defection method detailed in section 2.5, we need to verify the method. To do this, we replaced the CNT post with another piece of the Stablohm 650 wire and repeated the steps detailed in section 2.5. Because both the

wire and the post were the same material, the ratio of their elastic moduli, R, should equal one. We constructed a simple clamp using glass microscope slides to hold the post vertical under the microscope and taped another wire segment to the outside of the slides to use as a reference. With this set up we repeated the dual deflection test eight times.

To achieve as high an accuracy as possible, we very precisely measured the diameter of the wire and the lengths of both the wire and the post. We measured the diameter with a Mitutoyo digital micrometer and used the manufacturers listed diameter of 20 μm as a reference point. To measure the post and wire, we took an image in an optical microscope of a calibration slide and then took pictures of the post and wire at the same magnification and processed those images in Tracker, a video processing program that is explained in more detail in section 2.9. Figure 9 shows the measurement image of the wire with close ups of the clamping point, while Figure 10 shows images of the post and its clamping point. Using the close-up images of the clamping points, we made estimates on the uncertainty of each length. As seen in Figure 9, the exact clamping point of the wire is more ambiguous than the exact clamping point of the post. Therefore, the uncertainty in the wire length is slightly bigger than the uncertainty in the post length. These values are listed in Table 3 in section 3.3.

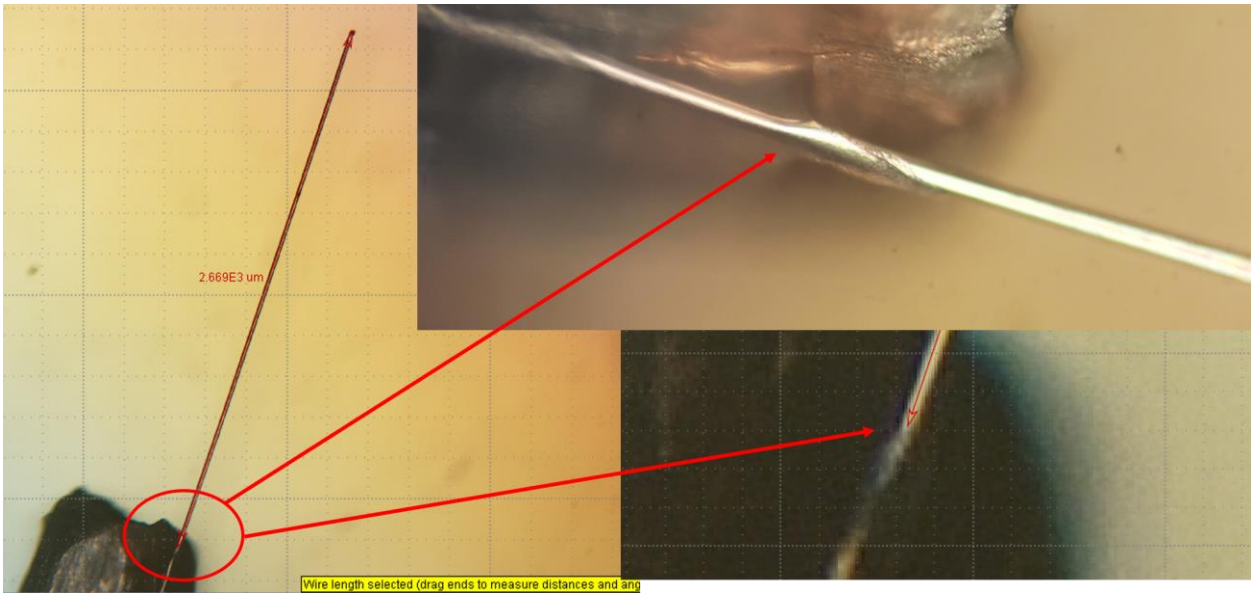

Figure 9: The measured wire used in the dual deflection method verification tests. The magnified views of the clamping points show the ambiguity in the exact clamping point of the glue.

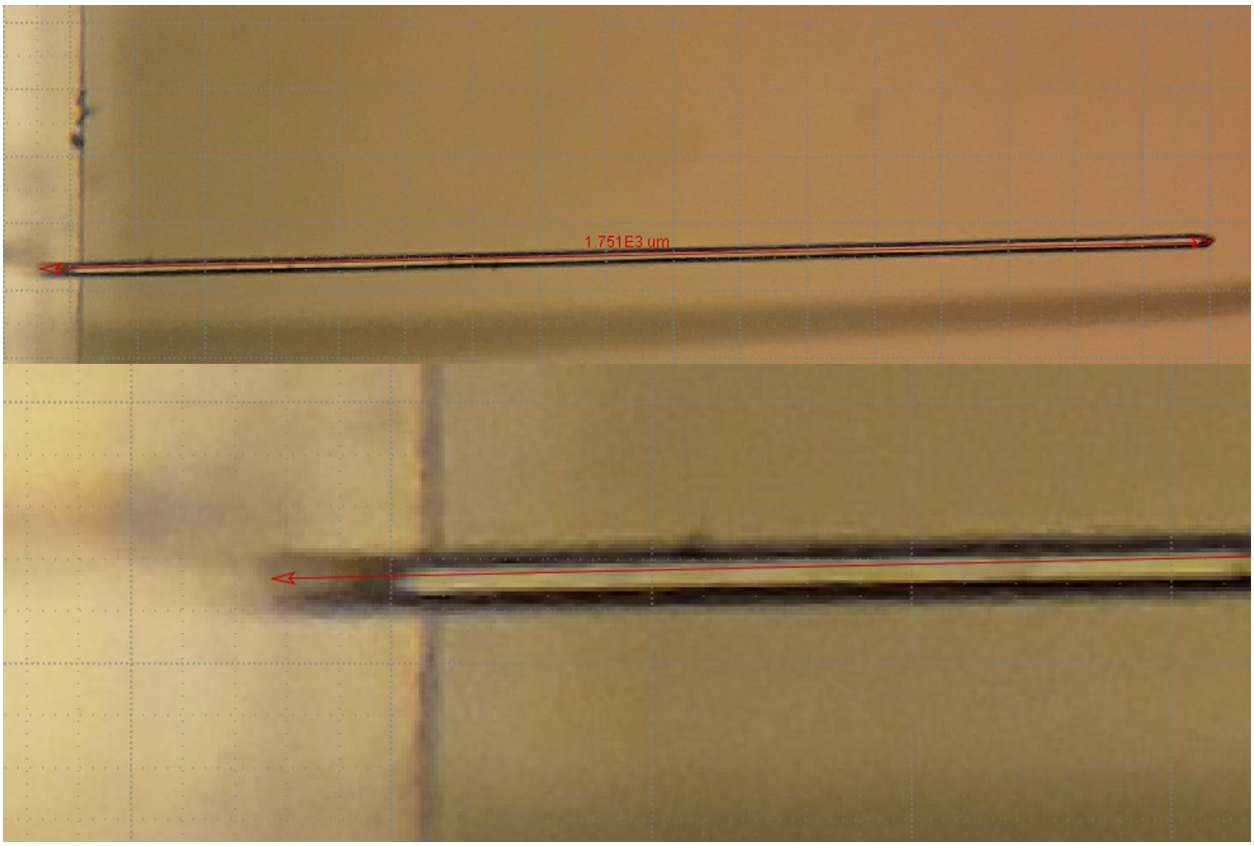

Figure 10: The measured post used in the dual deflection method verification testing. The magnified view of the clamping point between the glass slides shows a sharp cut off.

2.8 Wire 3-point bending tests

A well-defined stiffness of the wire is vital to the accurate measurement of the probe stiffness. Using an Instron 3345 tensile tester, I preformed extensive 3-point bending measurements on 20 µm diameter Stablohm 650 wire from California Fine Wire.[27] Figure 11 is a schematic for how this 3-point bending test is set up and implemented. For 3-point bending measurements to be accurate, the gap between the two support points must be 20 or more times the diameter of the wire. Additionally, the razorblade must make contact in the exact center of the supports, otherwise the test will measure a much higher stiffness. Therefore, we used a 600 µm gap and pressed the wire down into the center of that gap with a razorblade and measured the applied force vs. displacement as shown in Figure 15. I continued to press on the wire until the force displacement curve was no longer linear.

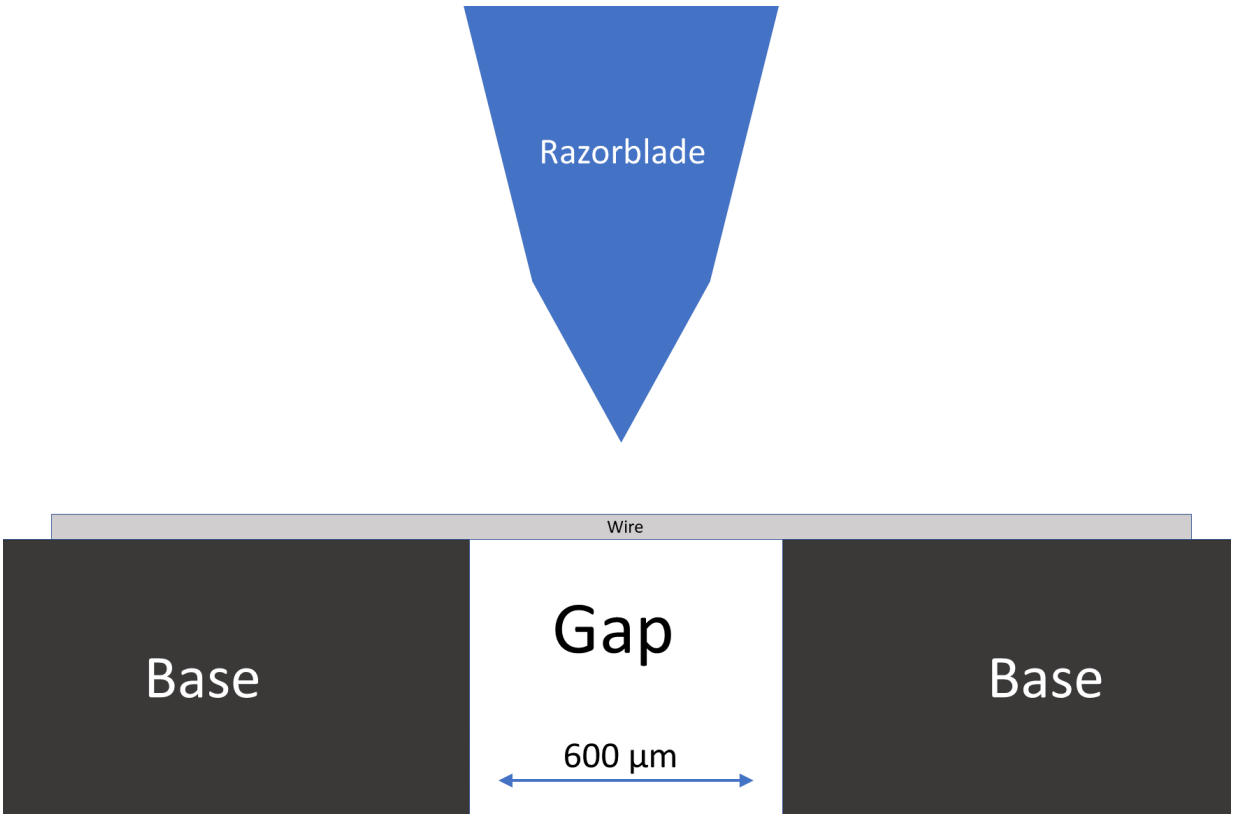

Figure 11: A schematic showing the 3-point bending test done on the Stablohm wire to calculate stiffness. The wire is the grey bar above the gap and has a diameter of 20 microns. The Instron machine lowers the razorblade and presses on the wire while measuring the force and displacement.

I repeated the 3-point bending test for 20 samples of the wire. I processed the force displacement curves in Excel by fitting the linear portion of the curve; the slope of that line fit is the stiffness for that sample. I averaged all 20 individual stiffnesses and used that average stiffness and standard deviation as the wire stiffness and error, respectively, in the Euler beam theory calculations to find modulus of the CNT probes. In section 3.2, the average wire stiffness and error are recorded along with a plot of the individual stiffness measurements in Figure 16.

The average stiffness is used as a reference to calculate the stiffness of the wire in **Error! Reference source not found.**.A that is used for the dual deflection testing detailed in section 2.5. Since the wire length from the 3-point bending and the wire length used in the dual deflection testing are not the same, the average stiffness must be scaled to accurately represent the dual

deflection interaction. The scaled stiffness is used in section 2.7 to calculate the force on the probe. The stiffness scaling and force calculation are shown in equations 2.6.1 and 2.7.2, respectively. In equation 2.6.1, k_w is the scaled stiffness of the wire, k_{ref} is the average stiffness from the 3-point bending tests, l_{ref} is the length of the gap, L is the length of the wire, and l is the distance from the point of contact between the probe and the wire to the tip of the wire such that $(L - l)$ is the effective wire length.

$$k_w = \frac{k_{avg}}{16}\left(\frac{l_{ref}}{L - l}\right)^3 \qquad 2.6.1$$

2.9 Video processing

After completing the dual deflection tests detailed in section 2.5, I imported the footage to an open source program called Tracker for processing. A frame from the footage imported into Tracker is shown in Figure 12. Before measuring probe and wire deflection in Tracker, I needed to establish scale bar, set coordinates, and measure the effective length of the wire. I set the scale bar as the width of the wire since it is always in focus and has a well-known diameter. To be accurate, I take a line scan of the wire and place the ends the calibration stick where the line scan measures the median brightness. That is, I place the calibration stick ends on the wire in the transition from wire to substrate, where the pixel brightness is halfway between bright substrate and dark wire. Next, I set the coordinate axes down in the bottom left corner of the screen so that all measurements take place in the first quadrant and are positive. I then proceeded to the frame where the wire contacts the target probe and created a measuring tape to measure the wire length offset, *i.e.*, the distance from the point of contact between the probe and the wire to the tip of the wire. I estimated the point of contact by counting the pixels and using the halfway mark. I

placed the other end of the measuring tape at the end of wire so that the tap runs along the edge of the wire.

Once the scale bar, the coordinate axes, and effective wire length are measured, I can measure probe and wire deflection. Note that the effective wire length changes with each probe contact and must be remeasured for each probe. First, I created an object called a "point mass", which allows the user to mark a location frame by frame to track an object by recording time and x and y position. To track the wire, I use Tracker's Autotracker function, which automatically tracks the object using pixel differences. First, I choose a key frame and select a template area that has distinct vertical and horizontal shapes. This helps keep the point mass centered on the point of contact between the wire and post. Autotracker automatically evolves the template image as the post deflects to maintain accuracy and if any points are misplaced by Autotracker, they can be manually moved to the proper position. Next, I created another point mass, and I autotracked the edge of a vertically adjacent probe that will serve as my reference probe over the same time frame as wire/probe object. Because the point of contact is between 10 – 30 μm below the surface of the probes, the reference probe has no sharp edge to focus on, but Autotracker was far better than a human at maintaining a consistent tracking point. An error of 5 μm, as reported in Table 3, is estimated for both the reference and the wire measurements. After completing both measurements, I took both objects—the wire/probe object and the reference post object—and exported them as CSVs to Excel. There, I zeroed the offset of both objects. Then, since the wire/probe object records how much the wire moved from its starting position, I calculated the distance the target probe moved by taking the absolute value of the difference between the reference and the wire as shown in equation 2.9.1. The normalized wire and post deflections are then plotted as a linear $y_p \; vs. \; y_w$ equation as detailed in section 2.5 and equation 2.5.3.

$$y_p = |y_w - x_{ref}| \quad 2.9.1$$

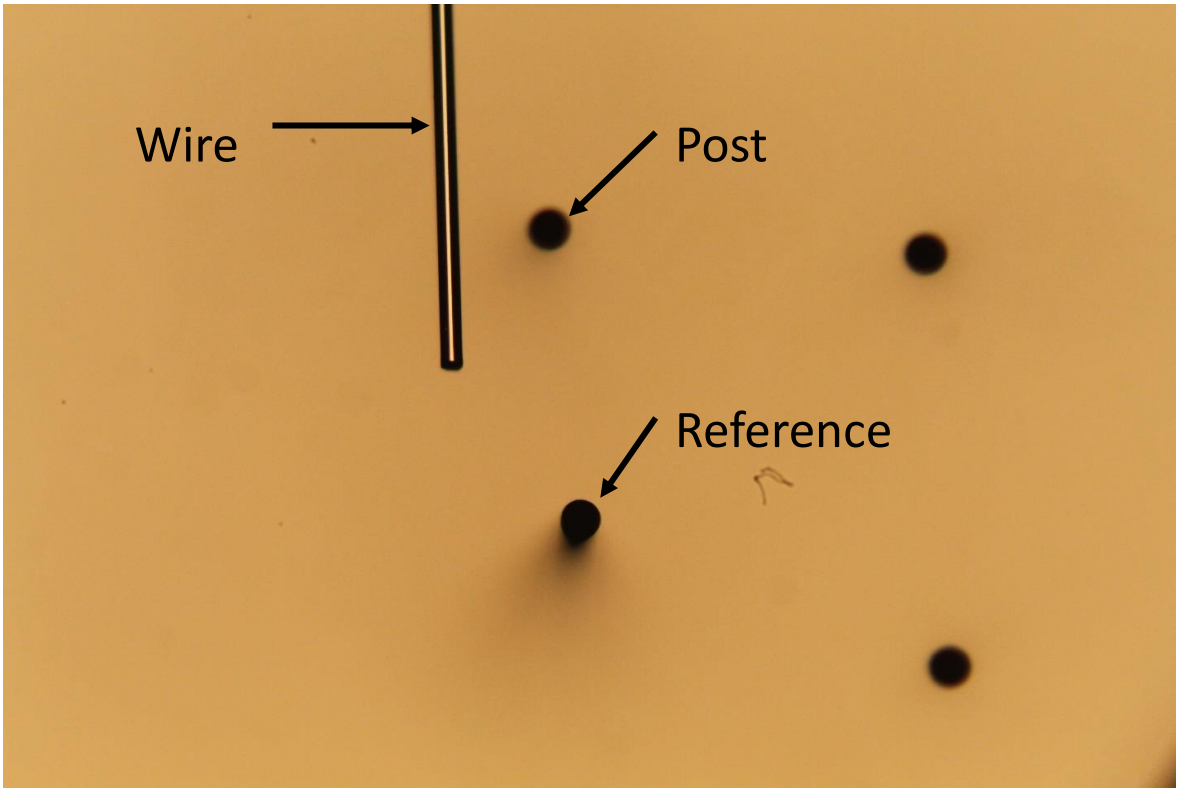

Figure 12: The recorded view of the dual deflection test. This footage is imported into Tracker.

Chapter 3: Results

3.1 Growth optimization results

The eight runs that JMP generated were repeated three times, with two additional runs for a total of 27 measured heights. These heights are shown in Figure 13, where the x-axis contains the specific conditions of the run, namely run temperature, growth gas flow rate, gas ratio, and iron thickness. Note the best runs—854 μm, 1023 μm, and 988 μm— consistently happened at

760˚C, 500 sccm, a H_2:C_2H_4 ratio of 1.1, and an iron thickness of 2 nm. This growth formula is used for all our CNT growths in the mechanical testing study *(see Table 2)*.

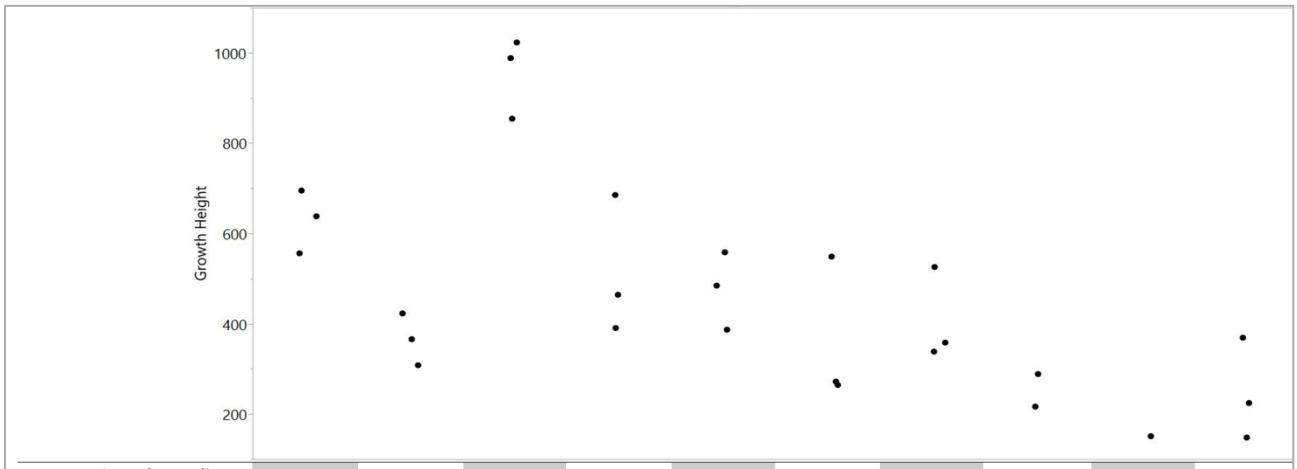

Temp (740 C˚, 760 C˚)	740 C˚	760 C˚	760 C˚	760 C˚	740 C˚	740 C˚	740 C˚	760 C˚	740 C˚	760 C˚
Flow Rate (500 sccm, 800 sccm)	500 sccm	800 sccm	500 sccm	500 sccm	800 sccm	800 sccm	500 sccm	800 sccm	800 sccm	800 sccm
Gas Ratio (H_2: C_2H_4) (0.9, 1.1)	0.9	0.9	1.1	0.9	1.1	0.9	1.1	0.9	1.1	1.1
Fe Thickness (2 nm, 4 nm)	2 nm	2 nm	2 nm	4 nm	2 nm	4 nm	4 nm	4 nm	4 nm	4 nm

Figure 13: The measured growth heights in microns from the CNT optimization study. The heights are categorized by the growth conditions the samples were grown under.

JMP produced a statistical analysis, called an effects summary, that evaluates the effect each variable had on growth height, as well a few second order interactions. This effects summary is shown in Figure 14. The bars show the log worth—the negative log of the p value—of each variable on the response, *i.e.*, the height of the CNT growth. Anything above the green line has a log worth of two, which is statistically significant. Therefore, while all variables have some impact on growth height, the CNT growth is dominated by the iron thickness, the gas flow rate, and the second order interaction between temperature and flow rate. Without a larger sample size with more varied runs, it is impossible to quantify the effect of gas ratio, temperature, or additional second order interactions on growth height.

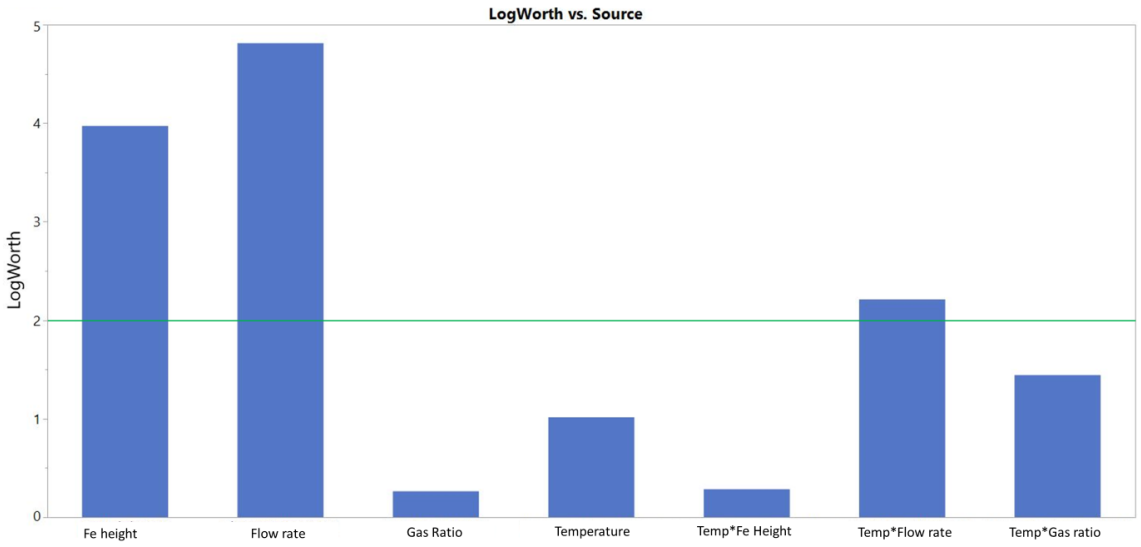

Figure 14: The effects summary of growth variables on CNT growth height. The three categories on the right are second order interactions of temperature with the other three variables. The y-axis plots the log worth, which is the log of the *p* value of each effect on the response. Anything above the green line is statistically significant.

3.2 Three-point bending results

Twenty three-point bending tests on a Stablohm 650 wire produced force/deflection curves, one of which is shown in Figure 15, from which we extracted the wire stiffnesses plotted in Figure 16. After averaging the twenty different tests, all of which are shown in Figure 16, we measured a stiffness 2214 N/m with an error of +/- 222 N/m. However, this stiffness results in a calculated elastic modulus that is six times bigger than the reported manufacturers value of 213 GPa and the generic nichrome modulus of 220 GPa. This discrepancy is probably due to the sensitivity of the razor blade placement; a slight displacement from exact center can drastically

increase the measured stiffness. Due to this complication, we decided to use the manufacture's reported elastic modulus instead of our calculated modulus.

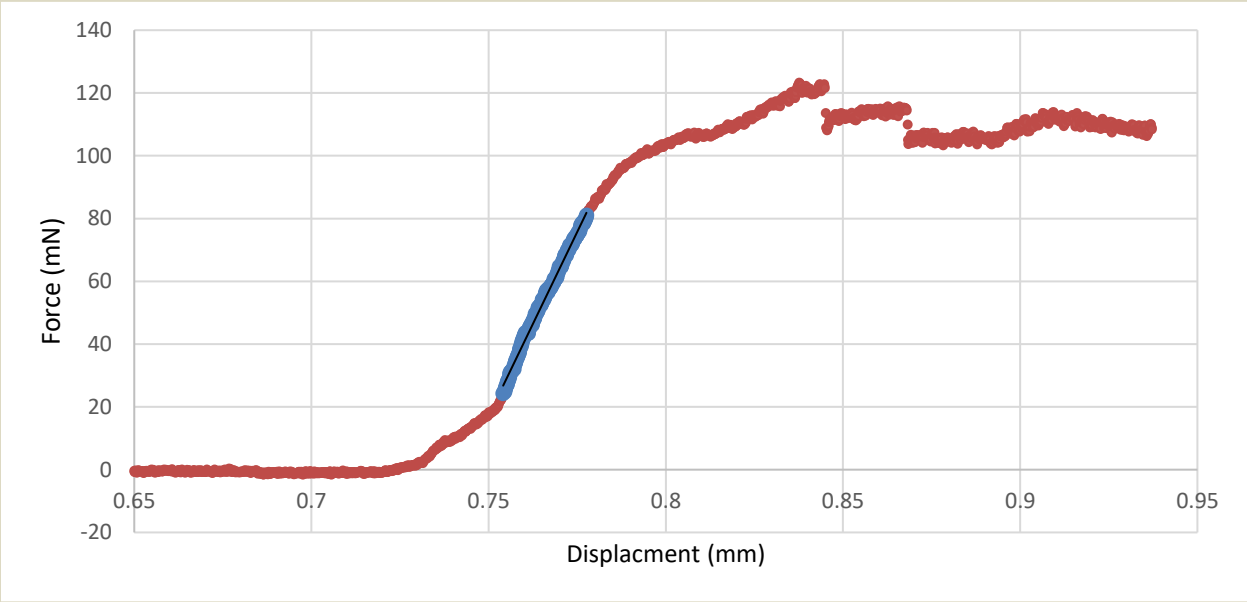

Figure 15: A force/displacement curve from one of the 3-point bending tests. The blue portion is the linear elastic region that was fitted with the trend line shown. The slope of that trendline is the measured stiffness of that sample.

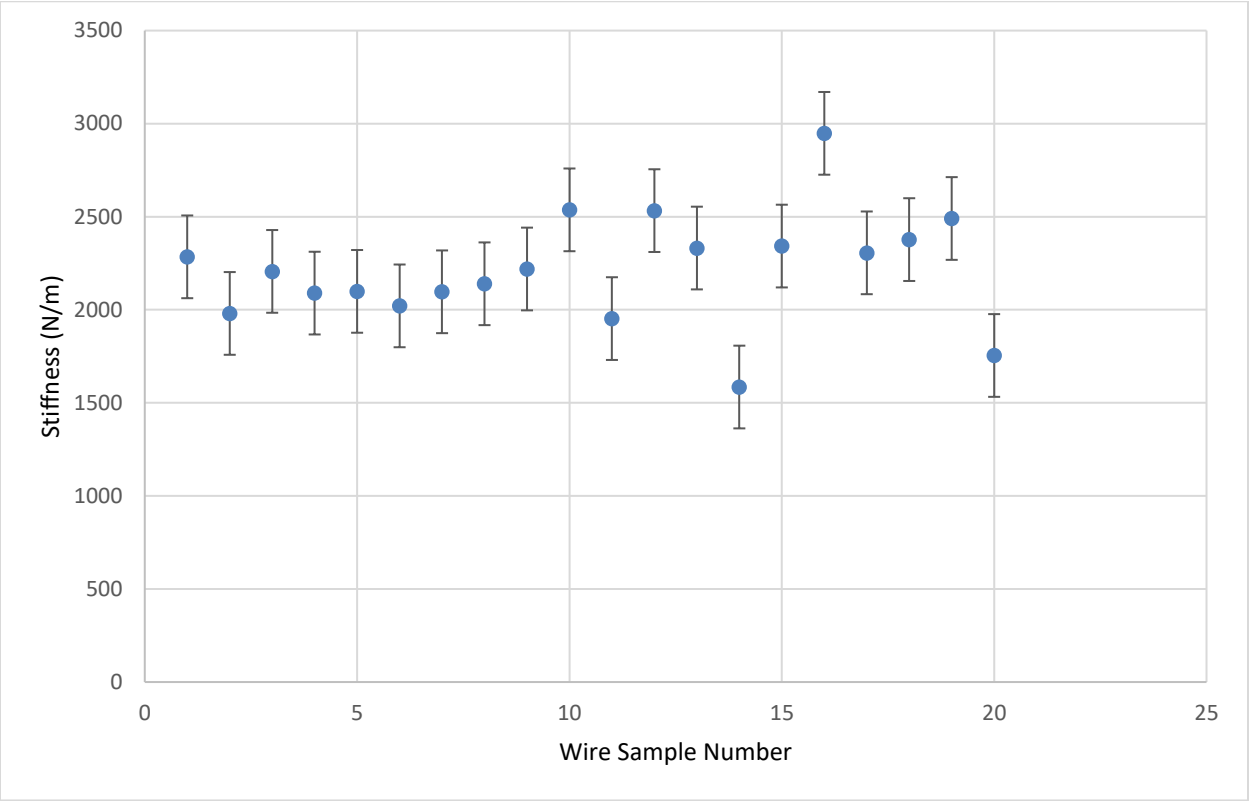

Figure 16: The measured wire stiffness from twenty 3-point bending tests done on an Instron.

3.3 Method verification and Uncertainty results

The theory detailed in section 2.7 states that the ratio of the modulus of the post and wire, R, should be equal to one since the moduli are the same. After running eight tests on the same post, the averaged ratio was $R = 0.908 \pm 0.349$, which puts the target of one within the error bars, thus verifying the method. The error was calculated using the method verification quantities and uncertainties in Table 3. A graph of the post vs. wire deflection from one run is shown in Figure 17.

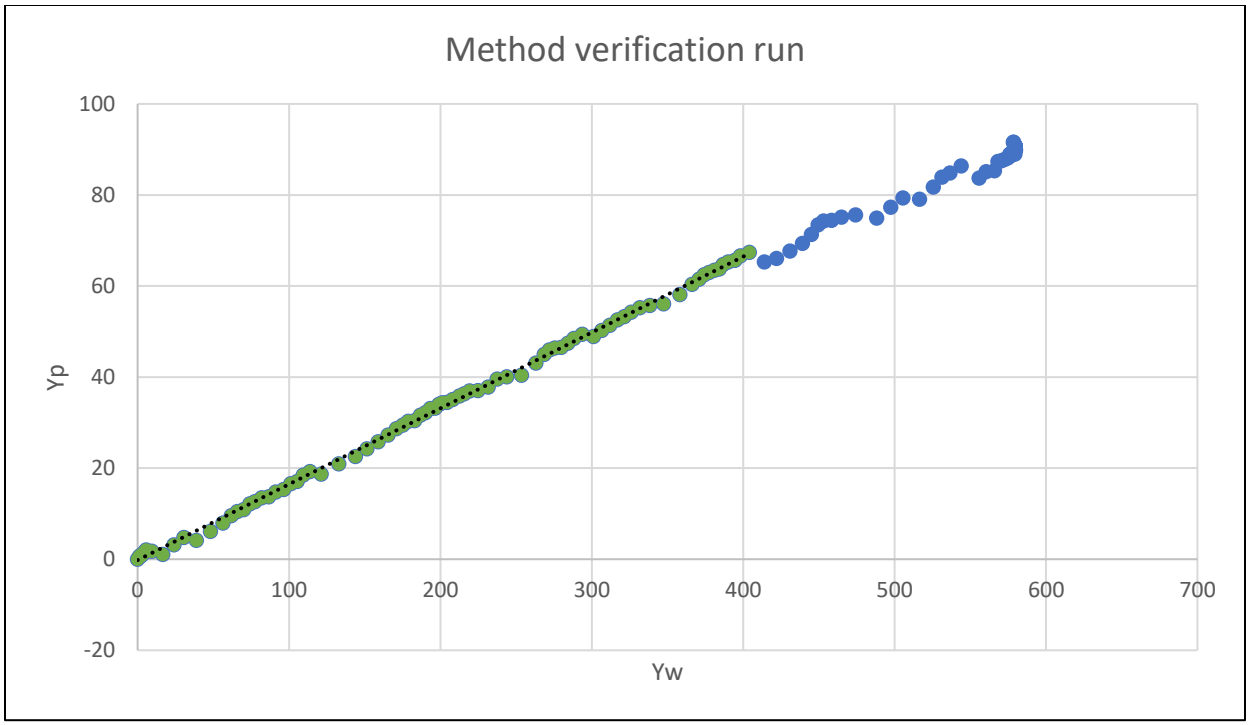

Figure 17: A graph of post deflection vs. wire deflection of a method verification run. The green section is used for Deming linear regression.

Quantity	*Value*	*Error*	*Percent Error*
x_{ref}	--	5 μm	--
y_w	--	5 μm	--
y_p	--	7.07 μm	--
d_w	20 μm	1.27 μm	6.35%
d_p $(method\ verification)$	20 μm	1.27 μm	6.35%
d_p $(CNT\ post)$	20 μm	1 μm	2.56%
$L_{w_{full}}$	2669 μm	100 μm	3.8%
$L_{w_{offset}}$	108 μm	5 μm	4.63%
L_w	2561 μm	100.13 μm	3.9%

$L_{w_{offset}}(\boldsymbol{CNT\ post\ average})$	205 μm	5 μm	2.4%
$L_w(\boldsymbol{CNT\ post\ average})$	2464 μm	100.13 μm	4.06%
$L_{p_{full}}$ $(\boldsymbol{method\ verification})$	1751 μm	30 μm	1.17%
$L_{p_{offset}}$ $(\boldsymbol{method\ verification})$	400 μm	5 μm	1.25%
L_p $(\boldsymbol{method\ verification})$	1351 μm	30.41 μm	2.25%
$L_{p_{full}}$ $(\boldsymbol{CNT\ post\ average})$	536 μm	5 μm	0.93%
$L_{p_{offset}}$ $(\boldsymbol{CNT\ post\ average})$	30 μm	5 μm	4.13%
L_p $(\boldsymbol{CNT\ post\ average})$	506 μm	7.07 μm	1.3%
$\boldsymbol{m}$ $(\boldsymbol{method\ verification\ average})$	0.161	0.00115	0.7%
$\boldsymbol{m}$ $(\boldsymbol{CNT\ post\ average})$	0.168	0.0007	0.4%
$\boldsymbol{R}$ $(\boldsymbol{method\ verification})$	0.904	0.349	38.4%
E_w	213 GPa	2.13 GPa	1%
E_p $(\boldsymbol{method\ verification\ average})$	194 GPa	74.6 GPa	38.4%
E_p $(\boldsymbol{CNT\ posts\ average})$	678 MPa	205 MPa	30.3%

Table 3: A complete list of all the errors and their percentage of the value. Any method verification quantity refers to the "post" wire. R does not have any significant meaning for CNT post measurements, so it is not included. Some percent errors are averages since the exact number changes for each run. x_{ref}, y_w and y_p percent errors are expressed in m percent error.

3.4 CNT Dual Deflection results

We measured 19 probes from the same CNT growth with the same set up and same wire length of 2600 μm +/- 100 μm. Since not all probes were straight in each growth, probes only qualified for measurement if the top of their growth did not deviate from their base by more than 20%. Among those probes measured, if the measured modulus was more than three standard

deviations from the mean, we threw out that data point. The mean measured modulus of the CNT probes was 678 MPa with an error of 30.3%. All values and their errors used to calculate the post modulus are recorded in Table 3. Figure 18 shows the graph of post deflection vs wire deflection for one of the measured posts. The orange portion is the portion used for linear regression. All other measured posts have similar graphs and those are included in the appendix.

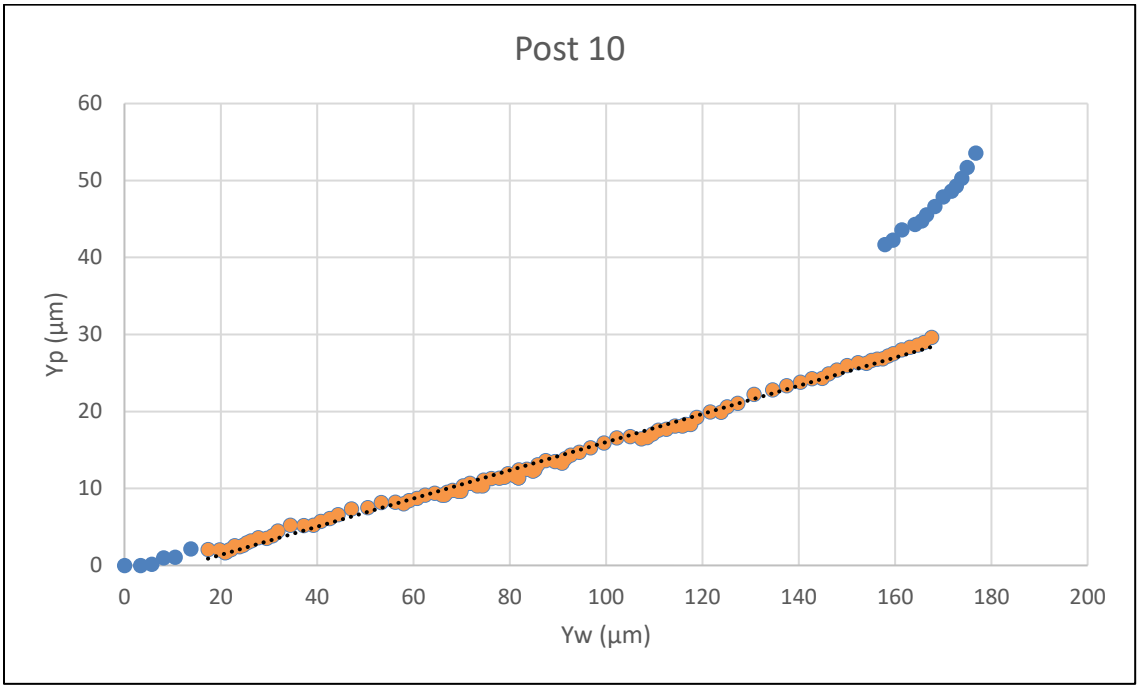

Figure 18: The deflection of a post vs the deflection of a wire. The orange portion is the linear section used to calculate the modulus of the post. The discontinuity is when the post fails.

3.5 Failure mechanisms

Upon flexing, one half of the probe is in compressive stress and the other half is in tension stress. This generates tension tears on one half of the base and compression buckles on the other half. **Error! Reference source not found.**Figure 19 shows the base of post after it was deflected. A shear void appeared in the center of the probe between the tension and compressive stresses. Since the probes are conglomerations of individual nanotubes, the stress is not uniform

throughout the structure. Stress concentrations are at the base and are focused on the shortest tubes first, then progress to longer tubes as the short tubes break. This is evident by the fuzzy, hairy appearance of the left-over stumps in Figure 20.

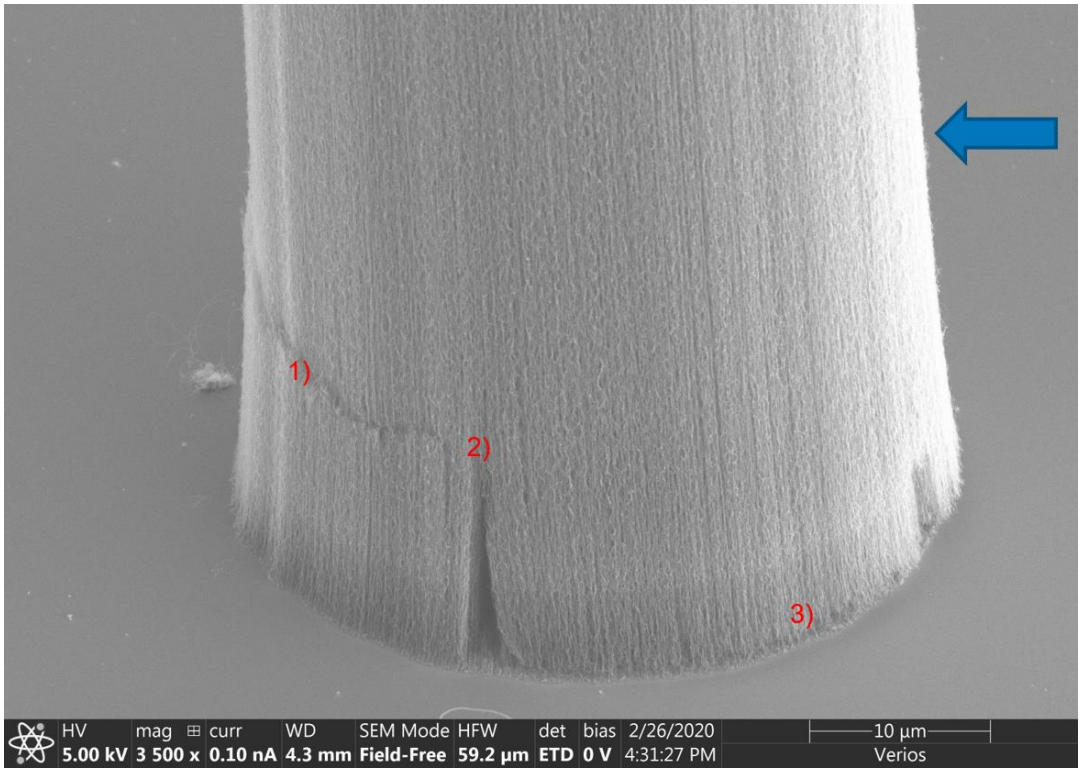

Figure 19:The base of a ~500 µm tall CNT probe that experienced a force in the left direction (direction of the arrow). Three failure mechanisms are visible: 1) the compression buckle on the left half of the base, 2) the shear tear in middle, and 3) a tension tear on the right side of the base.

This failure method rips the tension half of the probe off the substrate and creates a sort of hinge on the compression buckle. This was evident when after pushing on the probe until failure, upon pushing the probe in the same direction again, there are huge probe deflections with very little wire deflection. However, upon pushing the same probe in the opposite direction the probe snaps almost immediately, leaving a partial stump on the substrate which is seen in Figure 20. The tension tearing and compression buckling is evident in the post/wire deflections curve in Figure 18, where there is a discontinuous jump forward in probe deflection. The discontinuity

occurs because the failure of the post happens so quickly that the camera—which is filming at 30 frames/sec—often misses the break.

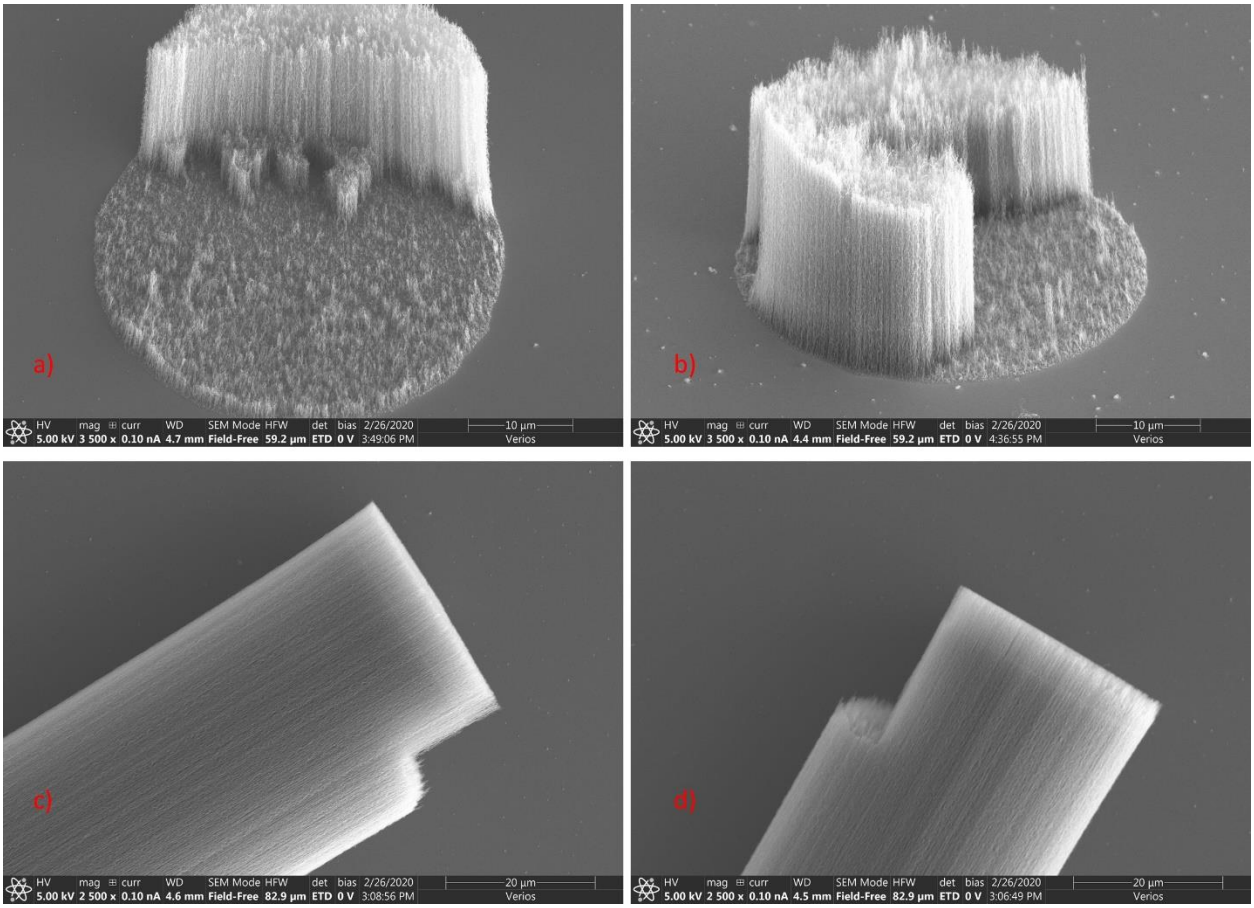

Figure 20: a) probe stump with torn CNT fibers. b) additional stump. c) detached probe with missing stump chunk. d) additional detached probe

Chapter 4: Discussion

4.1 Uncertainty sensitivity

There is a notable difference between the percent error of base measured quantities, *i.e.* diameter, length and deflection, and the final percent error of the post elastic modulus. This is

due largely to the weight that the diameter and length measurements carry in the error propagation. Because diameter is raised to the fourth power and length to the third, they have a disproportional and dominating effect on the total error, as shown in equation 2.6.6. The effect of the powered error is so strong that it completely dominates the error of R and consequently, the error in E_p, which is evident in Table 3 where the error in E_p $(method\ verification)$ is entirely decided by error in R.

Both length and diameter have a disproportional effect on the post modulus, but small changes in diameter—being the smaller dimension by two orders of magnitude when compared to the wire—can drastically alter the calculated modulus. For example, the wire has a diameter of 20 μm according to the manufacturer's specifications and the post modulus is 678 MPa; but, if the diameter is decreased by just a single micron, the CNT post modulus decreased by ~120 MPa, an 18% change. However, despite this extreme sensitivity to the diameter measurement, a 30% error is sufficient for our needs in reporting CNT elastic modulus values. Practically, the modulus is simply a guide when designing neural probes, since the stiffness of the probes can be reduced by reducing the diameter and elongating the probes.

4.2 CNT material viability for neural probes

The measured modulus of the probes, at 678 MPa, is comparable to invasive polymer probes being used today but does not compare to ultra-flexibility of hydrogel probes.[13] This may mean that hydrogel probes are the superior biocompatible material for invasive probes, but the CNT probes may yet prove to be a better biocompatible probe. For one, CNT MEMS probes achieve much higher aspect ratios than hydrogels can—a side effect of their low modulus—and can penetrate the cortex much further, accessing deeper neurons. Additionally, CNTs, as a raw

material, have shown promise at invasive biocompatibility.[28–31] The CNT probes could also be made more narrow, which would decrease overall stiffness. Stiffness might be more important for biocompatibility than actual elastic modulus as evidenced by ultra-thin polymer probes that have reasonable high moduli, but low stiffness in their minimum dimension.[2]

4.3 Additional challenges

One of the principle challenges is that while CNTs have shown promising biocompatible characteristics, they have—paradoxically—also shown carcinogenic effects.[32] There is currently not enough research to tip public opinion one way or another. More importantly, the FDA has been very slow to clear new neural probes for clinical human trials. The UEA was invented in the 70s, yet it is still the gold standard for invasive human testing, despite there being many more modern derivatives, illustrating the slow adoption rate of new neural probe technology.[4]

4.4 Future work

The next step for the BYU CNT neural probe array is examine the effect of carbon infiltration on the probe stiffness and modulus. The possibility of tuning stiffness to meet certain requirements is a unique advantage of the CNT neural probes. Additional next steps involve developing a working prototype that can be tested in animals. This will require extensive insertion testing and may require stiff water-soluble polymer coatings to properly insert into the brain. The insertion mechanism must be tested before *in vivo* testing can begin. However, *in vivo* data is necessary to confirm or refute the carcinogenic effects of CNTs implanted the brain. If animal testing shows promising biocompatibility, much more funding will be dedicated to CNTs as a biocompatible material for humans.

Appendix

Bibliography

1. D. Purves et al., “Summation of Synaptic Potentials,” Neurosci. 2nd Ed. (2001).
2. E. Musk and Neuralink, “An integrated brain-machine interface platform with thousands of channels,” bioRxiv, 703801 (2019) [doi:10.1101/703801].
3. “Six Paths to the Nonsurgical Future of Brain-Machine Interfaces,” <https://www.darpa.mil/news-events/2019-05-20> (accessed 1 February 2020).
4. “Advances in Penetrating Multichannel Microelectrodes Based on the Utah Array Platform. - Abstract - Europe PMC,” <https://europepmc.org/article/med/31729670> (accessed 17 April 2020).
5. Blackrock Microsystems, “UEA Neural Electrodes,” <https://www.blackrockmicro.com/electrode-main/> (accessed 1 February 2020).
6. R. A. Normann et al., “High-resolution spatio-temporal mapping of visual pathways using multi-electrode arrays,” Vision Res. **41**(10–11), 1261–1275 (2001) [doi:10.1016/s0042-6989(00)00273-x].
7. L. R. Hochberg et al., “Reach and grasp by people with tetraplegia using a neurally controlled robotic arm,” Nature **485**(7398), 372–375 (2012) [doi:10.1038/nature11076].
8. G. Chen et al., “Fabrication of High Aspect Ratio Millimeter-Tall Free-Standing Carbon Nanotube-Based Microelectrode Arrays,” ACS Biomater. Sci. Eng., acsbiomaterials.8b00038 (2018) [doi:10.1021/acsbiomaterials.8b00038].
9. “Utah Array |.”
10. R. Bhandari et al., “A wafer-scale etching technique for high aspect ratio implantable MEMS structures,” Sens. Actuators Phys. **162**(1), 130–136 (2010) [doi:10.1016/j.sna.2010.06.011].
11. F. Barz et al., “CMOS-compatible, Flexible, Intracortical Neural Probes,” IEEE Trans. Biomed. Eng., 1–1 (2019) [doi:10.1109/TBME.2019.2936740].
12. S. H. Felix et al., “Insertion of Flexible Neural Probes Using Rigid Stiffeners Attached with Biodissolvable Adhesive,” JoVE J. Vis. Exp.(79), e50609 (2013) [doi:10.3791/50609].
13. L. Luan et al., “Ultraflexible nanoelectronic probes form reliable, glial scar–free neural integration,” Sci. Adv. **3**(2), e1601966 (2017) [doi:10.1126/sciadv.1601966].
14. Z. Zhao et al., “Flexible deep brain neural probes based on a parylene tube structure,” J. Micromechanics Microengineering **28**(1), 015012 (2017) [doi:10.1088/1361-6439/aa9d61].
15. G. Kook et al., “Neural Probes for Chronic Applications,” Micromachines **7**(10) (2016) [doi:10.3390/mi7100179].
16. D. N. Hutchison et al., “Carbon Nanotubes as a Framework for High-Aspect-Ratio MEMS Fabrication,” J. Microelectromechanical Syst. **19**(1), 75–82 (2010) [doi:10.1109/JMEMS.2009.2035639].
17. C. by M. Ströck, *English: This illustration depicts eight of the allotropes (different molecular configurations) that pure carbon can take:* (2006).
18. C. Goze-Bac, “NMR studies of carbon nanotubes and derivatives” (2008).
19. “Carbon nanotube,” in Wikipedia (2020).
20. “Physicists grow micro-machines from carbon,” <https://phys.org/news/2011-03-physicists-micro-machines-carbon.html> (accessed 18 April 2020).
21. Y. Y. Wei et al., “Effect of catalyst film thickness on carbon nanotube growth by selective area chemical vapor deposition,” Appl. Phys. Lett. **78**(10), 1394–1396, American Institute of Physics (2001) [doi:10.1063/1.1354658].
22. “Ostwald ripening,” in Wikipedia (2020).
23. K. Hata, “A super-growth method for single-walled carbon nanotube synthesis,” Synth. Engl. Ed. **9**(3), 167–179 (2016) [doi:10.5571/syntheng.9.3_167].

24. SAS Institute Inc., “Design of Experiments Guide Second Edition,” SAS Institute Inc. (2017).
25. “Euler–Bernoulli beam theory,” in Wikipedia (2020).
26. Charles Zaiontz, “Deming Regression Basic Concepts,” 18 August 2020, <http://www.real-statistics.com/regression/deming-regression/deming-regression-basic-concepts/>.
27. “Stablohm 650 Wire,” <https://www.calfinewire.com/datasheets/100187-stablohm650.html> (accessed 25 March 2020).
28. A. Fraczek et al., “Comparative in vivo biocompatibility study of single- and multi-wall carbon nanotubes,” Acta Biomater. **4**(6), 1593–1602 (2008) [doi:10.1016/j.actbio.2008.05.018].
29. M. A. Correa-Duarte et al., “Fabrication and Biocompatibility of Carbon Nanotube-Based 3D Networks as Scaffolds for Cell Seeding and Growth,” Nano Lett. **4**(11), 2233–2236 (2004) [doi:10.1021/nl048574f].
30. D. A. X. Nayagam et al., “Carbon Nanotubes: Biocompatibility of Immobilized Aligned Carbon Nanotubes (Small 8/2011),” Small **7**(8), 981–981 (2011) [doi:10.1002/smll.201190025].
31. C. Grabinski et al., “Effect of particle dimension on biocompatibility of carbon nanomaterials,” Carbon **45**(14), 2828–2835 (2007) [doi:10.1016/j.carbon.2007.08.039].
32. S. Fukushima et al., “Carcinogenicity of multi-walled carbon nanotubes: challenging issue on hazard assessment,” J. Occup. Health **60**(1), 10–30 (2018) [doi:10.1539/joh.17-0102-RA].